

Investigating Physics Beyond the Standard Model via Semileptonic tau Decays



By

Faiza Khalid

(Registration No: 00000365041)

Department of Physics

School of Natural Sciences

National University of Sciences and Technology (NUST)

Islamabad, Pakistan

(2024)

Investigating Physics Beyond the Standard Model via Semileptonic tau Decays



By

Faiza Khalid

(Registration No: 00000365041)

A thesis submitted to the National University of Sciences and Technology, Islamabad,

in partial fulfillment of the requirements for the degree of

Master of Science in

Physics

Supervisor: Dr. Muhammad Ali Paracha

School of Natural Sciences

National University of Sciences and Technology (NUST)

Islamabad, Pakistan

(2024)

THESIS ACCEPTANCE CERTIFICATE

Certified that final copy of MS thesis written by **Faiza Khalid** (Registration No. **00000365041**), of **School of Natural Sciences** has been vetted by undersigned, found complete in all respects as per NUST statutes/regulations, is free of plagiarism, errors, and mistakes and is accepted as partial fulfillment for award of MS/M.Phil degree. It is further certified that necessary amendments as pointed out by GEC members and external examiner of the scholar have also been incorporated in the said thesis.


Signature:  _____

Name of Supervisor: Dr. Muhammad Ali Paracha

Date: 15-08-2024

Signature (HoD): ^{for}  _____

Date: 15/8/2024

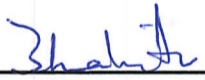
Signature (Dean/Principal):  _____

Date: 15.8.2024

National University of Sciences & Technology**MS THESIS WORK**

We hereby recommend that the dissertation prepared under our supervision by: Faiza Khalid, Regn No. 00000365041 Titled: Investigating Physics beyond the Standard Model via Semileptonic tau Decays be Accepted in partial fulfillment of the requirements for the award of **MS** degree.

Examination Committee Members1. Name: DR. SAADI ISHAQSignature: 2. Name: DR. FASIAL MUNIR BHUTTASignature: Supervisor's Name Dr. Muhammad Ali ParachaSignature: 

^{for}

Head of Department

15/8/2024
Date

COUNTERSIGNEDDate: 15.8.2024


Dean/Principal

DEDICATION

This thesis is dedicated to *my beloved parents*

ACKNOWLEDGEMENTS

First and foremost, I have to thank Allah Almighty for His blessings. I am grateful to everyone who has supported and guided me throughout my Master's journey. I extend my deepest gratitude to my advisor, **Dr. Muhammad Ali Paracha**, for his time, valuable suggestions, and constructive criticism, which have significantly improved the quality of this thesis. As his research assistant, I benefited immensely from his expertise and mentorship, which have played an important role in completing this work. On a personal note, I am grateful to my family and friends for their support and constant encouragement. Your support and encouragement have provided a much-needed balance between work and leisure.

Contents

LIST OF FIGURES	VI
ABSTRACT	IX
1 Introduction	1
2 Theoretical Framework	4
2.1 Lagrangian of the Standard Model	4
2.2 Spontaneous Symmetry Breaking	6
2.3 Hadronic Decay Modes of the τ Lepton	8
2.3.1 Single Hadron Decays	10
2.3.2 Two Hadron Decays	10
2.4 Effective Field Theory	11
3 Investigating τ Decays using Effective Field Theory	15
3.1 Effective Field Theory as a Tool to Investigate τ Decays	15
3.2 The Framework of Effective Field Theory	16
3.3 Chiral Symmetry	17
3.3.1 Formulating the Chiral Lagrangian in QCD	18
3.4 Chiral Perturbation Theory (ChPT)	20
3.4.1 Extended QCD Lagrangian	20
3.4.2 Chiral Symmetry Transformations and Effective Lagrangian	21
3.4.3 Noether Currents and Generating Functional	22
3.4.4 Power Counting	22
3.5 Resonance Chiral Theory (RChT)	23
3.5.1 Inclusion of Resonances	23
3.5.2 Lagrangian Formulation	23
3.6 Form Factors in τ Decays	24
4 Probing New Physics via $\tau^- \rightarrow \pi^- \eta^{(\prime)} \nu_\tau$ Decays	26
4.1 Amplitude of $\tau^- \rightarrow \pi^- \eta^{(\prime)} \nu_\tau$ Decays	26

4.2	$\pi^-\eta^{(\prime)}$ Scalar Form Factor Using Breit-Wigner approach	29
4.3	Vector Form Factor for $\pi^-\eta^{(\prime)}$	33
4.4	Tensor Form Factor (TFF) for $\pi^-\eta^{(\prime)}$	34
4.5	Physical Observables	35
4.5.1	Dalitz plots	36
4.5.2	Angular Distribution	37
4.5.3	Decay Width	38
4.5.4	Forward-Backward Assyemtry (A_{FB})	39
5	Phenomenological Analysis of $\tau^- \rightarrow \pi^-\eta^{(\prime)}\nu_\tau$ Decays	41
5.1	Dalitz Plot Analysis	41
5.2	Differential Decay Rate Analysis	47
5.2.1	Analysis of $\tau^- \rightarrow \pi^-\eta\nu_\tau$ Decay	47
5.2.2	Analysis of $\tau^- \rightarrow \pi^-\eta'\nu_\tau$ Decay	49
5.3	Forward-Backward Asymmetry Analysis	51
6	Conclusion	54

List of Figures

2.1	(a) $\mu^2 > 0$: the ground state is uniquely located at $\phi = 0$, maintaining the U(1) symmetry of the Lagrangian (b) $\mu^2 < 0$: the ground state becomes degenerate, with each ground state breaking the U(1) symmetry of the Lagrangian [1].	7
2.2	(a) In the Standard Model, integrating out the W boson yields an effective four-fermion interaction. (b) The two crossed circles indicate a local four-quark operator within the EFT [2]	14
3.1	The diagrams that contribute to the axial-vector form factors of hadrons [3].	25
3.2	Theoretical $M_{\pi\pi\pi}^2$ spectra for the $\tau^- \rightarrow \pi^- \pi^- \pi^+ \nu_\tau$ decay are compared with the experimental results from ALEPH [4].	25
4.1	Feynman Diagram at Tree-Level for $\tau^- \rightarrow \pi^- \eta^{(\prime)} \nu_\tau$ Decays	27
4.2	The normalized scalar form factor for $\pi^- \eta'$, derived using the Breit-Wigner approach outlined in Section 4.2	31
4.3	The Breit-Wigner method, detailed in Section 4.2, yielded normalized $\pi^- \eta'$ scalar form factors with two resonances (red dashed curve) and one resonance (solid black curve), respectively.	32
4.4	The Breit-Wigner method, detailed in Section 4.2, yielded normalized $\pi^- \eta$ scalar form factors with two resonances (red dashed curve) and one resonance (solid black curve), respectively.	33
4.5	$\pi^- \eta^{(\prime)}$ VFF as obtained by using Breit-Wigner approach	34
4.6	The vector form factor $\pi^- \pi^0$ found by the Belle Collaboration	35
5.1	Dalitz plot distributions of $ \mathcal{M} ^2$ for the decay $\tau^- \rightarrow \pi^- \eta' \nu_\tau$. The figures show the distributions for the (a) Standard Model ($\hat{\epsilon}_S = \hat{\epsilon}_T = 0$), (b) $\hat{\epsilon}_S = 0.006, \hat{\epsilon}_T = 0$, and (c) $\hat{\epsilon}_S = 0, \hat{\epsilon}_T = 0.3$	42
5.2	Dalitz plot distributions of $ \mathcal{M} ^2$ for the decay $\tau^- \rightarrow \pi^- \eta \nu_\tau$. The figures show the distributions for the (a) Standard Model ($\hat{\epsilon}_S = \hat{\epsilon}_T = 0$), (b) $\hat{\epsilon}_S = 0.002, \hat{\epsilon}_T = 0$, and (c) $\hat{\epsilon}_S = 0, \hat{\epsilon}_T = 0.3$	43

5.3	Differential decay width distributions for the decay $\tau^- \rightarrow \pi^- \eta' \nu_\tau$ in $(s, \cos \theta)$ variables. The figures show the distributions for the (a) Standard Model ($\hat{\epsilon}_S = \hat{\epsilon}_T = 0$), (b) $\hat{\epsilon}_S = 0.006, \hat{\epsilon}_T = 0$, and (c) $\hat{\epsilon}_S = 0, \hat{\epsilon}_T = 0.3$	45
5.4	Differential decay width distributions for the decay $\tau^- \rightarrow \pi^- \eta \nu_\tau$ in $(s, \cos \theta)$ variables. The figures show the distributions for the (a) Standard Model ($\hat{\epsilon}_S = \hat{\epsilon}_T = 0$), (b) $\hat{\epsilon}_S = 0.002, \hat{\epsilon}_T = 0$, and (c) $\hat{\epsilon}_S = 0, \hat{\epsilon}_T = 0.3$	46
5.5	Distribution of the total differential decay width for $\tau^- \rightarrow \pi^- \eta \nu_\tau$ plotted against the invariant mass. The SM utilizes a Breit-Wigner formula using two resonances (black line), while scenarios with $\hat{\epsilon}_S = 0.005, \hat{\epsilon}_T = 0$ are represented by a red dotted line, and $\hat{\epsilon}_S = 0, \hat{\epsilon}_T = 0.3$ by a blue dashed line.	48
5.6	The figure depicts the distribution of the invariant mass of the $\eta' \pi^-$ system for the Standard Model (black line) and scenarios with $\hat{\epsilon}_S = 0.005, \hat{\epsilon}_T = 0$ (red dotted line), and $\hat{\epsilon}_S = 0, \hat{\epsilon}_T = 0.3$ (blue dashed line). The axes are scaled in units of GeV^2	49
5.7	The figure depicts the distribution of the invariant mass of the $\eta' \pi^-$ system for the Standard Model (black line) and scenarios with $\hat{\epsilon}_S = 0.005, \hat{\epsilon}_T = 0$ (red dotted line), and $\hat{\epsilon}_S = 0, \hat{\epsilon}_T = 0.3$ (blue dashed line). The axes are scaled in units of GeV^2	50
5.8	Comparison of A_{FB} for the decay $\tau^- \rightarrow \pi^- \eta' \nu_\tau$ for $\hat{\epsilon}_S = 0.002, \hat{\epsilon}_T = 0$ (red line) and for $\hat{\epsilon}_S = 0, \hat{\epsilon}_T = 0.3$ (blue line) against the Standard Model prediction (black line).	51
5.9	Comparison of A_{FB} for the decay $\tau^- \rightarrow \pi^- \eta \nu_\tau$ with $\hat{\epsilon}_S = 0.002, \hat{\epsilon}_T = 0$ (red line) and $\hat{\epsilon}_S = 0, \hat{\epsilon}_T = 0.3$ (blue line) against the Standard Model prediction (black line).	52

List of Abbreviations

Abbreviations

SM	Standard Model
BSM	Beyond the Standard Model
NP	New Physics
FCC	First Class Current
SCC	Second Class Current
SFF	Scalar Form Factor
VFF	Vector Form Factor
TFF	Tensor Form Factor
ChPT	Chiral Perturbation Theory
RChT	Resonance Chiral Theory
A_{FB}	Forward-Backward Asymmetry
SSB	Spontaneous Symmetry Breaking
EFT	Effective Field Theory
QFT	Quantum Field Theory
QED	Quantum Electrodynamics
QCD	Quantum Chromodynamics
BR	Branching Ratio
CL	Confidence Level

CKM	Cabibbo-Kobayashi-Maskawa
GIM	Glashow-Iliopoulos-Maiani
LHC	Large Hadron Collider
CLEO	Cornell Laboratory for Elementary-particle Operations
LO	Leading-Order
VEV	Vacuum Expectation Value

Abstract

We examine the rare decays $\tau^- \rightarrow \pi^- \eta^{(\prime)} \nu_\tau$ that are G-parity suppressed within the Standard Model and provide valuable insights into new physics through interactions beyond the SM. In this study, we used an effective field theory framework to investigate the sensitivity of various observables associated with these decays, incorporating interactions within the Standard Model fields up to six-dimensional operators, under the assumption of massless and left-handed neutrinos. Our findings indicate that the examined observables can effectively explain the underlying dynamics of these decays, showing significant sensitivity to scalar and tensor couplings. Upcoming experiments such as Belle II, LHCb upgrades, and future electron-positron colliders aim to investigate τ decays with high accuracy, potentially uncovering new physics beyond the Standard Model.

Chapter 1

Introduction

Weak currents can be divided into two categories specifically as first-class current (FCC) and second-class current (SCC), based on J^{PG} values of the decay current, as explained in [5] by Weinberg. Here, G -parity is a multiplicative quantum number resulting from the combined operation of isospin rotation and charge conjugation, symbolized as $G = Ce^{i\pi I_2}$, where C signifies charge conjugation and I_i represents the components of isospin rotation operators. According to the Standard Model, decays are predominantly influenced by FCC, which have J^{PG} values of 0^{++} , 0^{--} , 1^{+-} , 1^{-+} , and so on, and are characterized by $PG(-1)^J = +1$. On the other hand, SCC, which has J^{PG} values of 0^{+-} , 0^{-+} , 1^{++} , 1^{--} , and so on, are expected to be negligible and vanish when perfect isospin symmetry is achieved. Rare processes are particle decay modes hindered by approximation symmetries in the SM. They are an excellent approach for investigating new physics because their low amplitudes may closely resemble the indirect effects of new particles and interactions. Understanding and controlling the uncertainties within the Standard Model is critical for determining the influence of NP on the quantitative analysis conducted at flavor factories. This work centers on the phenomenology surrounding hadronic τ decays. The τ lepton is the heaviest known lepton and is the only one capable of decaying into hadrons. The decay mechanism is facilitated by the W^- boson, which mediates two weak charged currents. This makes it an excellent way to test electroweak interactions. Moreover, a complex and varied hadronic energy spectrum is observed due to the emission of a neutrino during the decay. This spectrum is generated by the weak quark current and can be used to study strong interactions at different energy levels. For this, semileptonic τ decays offer an ideal setting for studying non-perturbative Quantum Chromodynamics. They provide a platform for examining form factors, investigating the hadronization processes of QCD currents, and determining resonance parameters. These rare τ lepton's decay channels are becoming increasingly important in upcoming B-factory experiments, promising new insights into particle physics phenomena. These channels

have suppressed interactions and increased sensitivity to NP. In SM, several factors contribute to suppressing rare τ decays:

- Cabbibo suppression refers to the phenomenon where strange hadronic final states are relatively suppressed compared to non-strange ones in certain processes. This occurs when the CKM matrix element V_{us} is used instead of V_{ud} . Examples include $\tau^- \rightarrow K^- \eta' \nu_\tau$ and $\tau^- \rightarrow K^- \eta \nu_\tau$ [6, 7].
- Phase-space suppression is a common phenomenon in decays where final states involve kaons, η' , or η mesons, primarily due to the substantial masses of these particles. Furthermore, second-class current decays violate G -parity, wherein the vector current's G -parity opposes that of the hadronic system. In the isospin limit, G -parity is precisely conserved, hence such processes are not allowed in the Standard Model. Nevertheless, isospin serves as an approximate symmetry, it breaks down due to differences in electric charge and mass between up and down quarks, which leads to the suppression of these decays.

Our work focuses on the investigation of the rare SCC observed in $\tau^- \rightarrow \pi^- \eta^{(\prime)} \nu_\tau$ decays, as described in the reference [8]. We have two goals: first, to understand the hadronic form factors involved in the decay process, and second, to predict the resulting decay spectra and branching ratios. We hope that these predictions will encourage experimental collaborations to carry out measurements of these decays. We are studying certain processes using an effective Lagrangian framework. Within this framework lies an extensive Lagrangian composed of six-dimensional operators corresponding to left-handed neutrino fields. These operators encapsulate the effects of New Physics. Previous studies that focused on estimating the branching fractions within the ranges of $10^{-5} \sim 10^{-6}$ ($10^{-6} \sim 10^{-8}$) for the η (η') decay channels [9], also explored the invariant mass distribution as part of specific beyond the SM methodologies [10]. Predictions including the scalar form factor's (SFF) contribution introduce a notable source of uncertainty in most evaluations. As a result, a thorough understanding of the SFF is required to evaluate the potential impact of non-standard model effects. We expect that a detailed analysis of numerous observables in the $\tau^- \rightarrow \eta(\eta') \pi^- \nu_\tau$ decays at forthcoming superflavor factories will be particularly beneficial in distinguishing NP effects from isospin-violating contributions in the Standard Model.

The present experimental limits on the $\tau^- \rightarrow \eta \pi^- \nu_\tau$ decays from the BaBar [11], Belle [12], and CLEO [13] collaborations are: the branching ratio is less than 9.9×10^{-5} at a 95% confidence level (CL), less than 7.3×10^{-5} at a 90% CL, and less than 1.4×10^{-4} at a 95% CL, respectively. These upper bounds closely correspond to the Standard Model predictions are based on isospin breaking. The

BaBar collaboration set a limit of $< 7.2 \times 10^{-6}$ at a 95% confidence level (CL) for $\tau^- \rightarrow \eta' \pi^- \nu_\tau$ decays [14], whereas Belle obtained $< 4.6 \times 10^{-6}$ at a 90% CL [15] (previously, CLEO established an upper bound of 7.4×10^{-5} at a 90% CL [16]). Upcoming experiments at the intensity frontier, such as Belle II, aim to accumulate a significant amount of data, with a target of 4.5×10^{10} τ lepton pairs in their complete dataset. These experiments gave the first measurements of the $\tau^- \rightarrow \eta(\eta') \pi^- \nu_\tau$ decays [17].

The thesis is structured as: Chapter 2 introduces a theoretical framework that covers the Lagrangian of the Standard Model, Spontaneous Symmetry breaking, and hadronic decays of τ lepton. We will discuss exploring τ decays using Effective Field Theory in Chapter 3. Initially, we formulate the effective Lagrangian, which serves as the foundation of this thesis. Subsequently, we discuss the ChPT, which is employed in form factors. The formalism for rare τ decays is presented in Chapter 4. First, we write the amplitude of our decay, and then the definition of the hadronic matrix element is outlined by incorporating scalar, vector, and tensor form factors, followed by an expression describing the differential decay width. We will discuss these form factors using RChT. In Chapter 5, we conduct a numerical analysis of our research, which includes Dalitz plots and differential decay width distribution. Furthermore, forward-backward asymmetry plots are presented in this chapter. In Chapter 6, we conclude our thesis.

Chapter 2

Theoretical Framework

In this chapter, we will have an overview of the Standard Model Lagrangian, followed by a brief explanation of spontaneous symmetry breaking and the Higgs mechanism's role in generating particle masses. It then discusses the hadronic decays of the τ lepton and introduces the concept of Effective Field Theory.

2.1 Lagrangian of the Standard Model

The Standard Model (SM) of particle physics is a highly successful theoretical framework that explains the fundamental components of the universe and their interactions. The Lagrangian of SM stands as the most comprehensive and renormalizable equation, maintaining invariance under local gauge transformations corresponding to the symmetry group $SU(3)_C \times SU(2)_L \times U(1)_Y$. This structure requires a total of twelve gauge fields: eight G_μ^a from $SU(3)_C$, three W_μ^b from $SU(2)_L$, and one B_μ from $U(1)_Y$. The matter components within this equation transform according to either the fundamental or the trivial formulation of these symmetries. For clarity, Greek letters represent indices for the $SU(3)_C$ color group, capital letters denote family indices, and explicit columns are used to depict n -plets in $SU(2)_L$. Thus, the fundamental matter components of the Standard Model are structured as [18]:

$$\begin{aligned} l_N &= \begin{pmatrix} \nu_L \\ l_L \end{pmatrix}_N, & e_N &= l_{R,N}, & \phi &= \begin{pmatrix} \phi^+ \\ \phi^0 \end{pmatrix}, \\ q_{\alpha N} &= \begin{pmatrix} u_L \\ d_L \end{pmatrix}_{\alpha N}, & d_{\alpha N} &= d_{R,\alpha N}, & u_{\alpha N} &= u_{R,\alpha N} \end{aligned} \tag{2.1}$$

The $SU(2)_L$ group represents left-handed fields as doublets and right-handed fields as singlets. Here, the indexes α and N have values ranging from 1 to 3.

The scalar boson doublet is represented by ϕ , while the remaining particles are fermions. Their hypercharges are:

$$\begin{aligned} Y(l_N) &= -\frac{1}{2}, & Y(e_N) &= -1, & Y(\phi) &= \frac{1}{2}, \\ Y(q_{\alpha N}) &= \frac{1}{6}, & Y(d_{\alpha N}) &= -\frac{1}{3}, & Y(u_{\alpha N}) &= \frac{2}{3} \end{aligned} \quad (2.2)$$

The given expression:

$$\mathcal{L} = \mathcal{L}_F + \mathcal{L}_B + \mathcal{L}_S + \mathcal{L}_Y \quad (2.3)$$

represents the total Lagrangian density of the Standard Model, which is composed of four main components.

1. \mathcal{L}_F is the fermionic part which describes the behavior and interactions of fermions. It includes the kinetic terms for the fermion fields and their interactions with gauge bosons through covariant derivatives.

$$\mathcal{L}_F = \sum_N (\bar{l}_N \not{D} l_N + \bar{q}_N \not{D} q_N + \bar{e}_N \not{D} e_N + \bar{u}_N \not{D} u_N + \bar{d}_N \not{D} d_N) \quad (2.4)$$

where l_N and e_N typically represent the lepton fields, l_N denotes the neutrino and charged lepton doublets, and e_N represents the charged lepton singlets. q_N , d_N , and u_N usually represent the quark fields. These fields come in three color states: red, green, and blue. These color states are often represented as vectors, which is why they're referred to as color vectors and \not{D} represents a Dirac operator, which is a derivative operator acting on fermion fields in the context of quantum field theory:

$$\not{D} = \gamma^\mu D_\mu \quad (2.5)$$

where γ^μ are the Dirac gamma matrices, and D_μ is the covariant derivative, defined as:

$$D_\mu = I\partial_\mu + ig_s \frac{\lambda^a}{2} G_\mu^a + ig \frac{\sigma^b}{2} W_\mu^b + ig' B_\mu \quad (2.6)$$

as a result, each term is associated with a particle only when the particle exists within the fundamental representation of a corresponding symmetry.

2. \mathcal{L}_B is the gauge boson part that contains the kinetic terms governing the gauge fields (the force carriers: photons, W and Z bosons, and gluons) and describes their self-interactions. It is derived from the field strength tensors of the gauge fields.

$$\mathcal{L}_B = -\frac{1}{4} G_{\mu\nu}^a G_a^{\mu\nu} - \frac{1}{4} W_{\mu\nu}^b W_b^{\mu\nu} - \frac{1}{4} B_{\mu\nu} B^{\mu\nu} \quad (2.7)$$

where

$$G_{\mu\nu}^a = \partial_\mu G_\nu^a - \partial_\nu G_\mu^a - g_s f^{abc} G_\mu^b G_\nu^c \quad (2.8)$$

$$W_{\mu\nu}^b = \partial_\mu W_\nu^b - \partial_\nu W_\mu^b - g\epsilon^{abc} W_\mu^c W_\nu^b \quad (2.9)$$

$$B_{\mu\nu} = \partial_\mu B_\nu - \partial_\nu B_\mu \quad (2.10)$$

3. \mathcal{L}_S - Scalar (Higgs) part that governs the behavior of the Higgs field. This sector explains the dynamics of the Higgs field itself, including its potential energy and kinetic terms, as well as its interactions with gauge fields. It is expressed as follows:

$$\mathcal{L}_S = (D_\mu \phi)^\dagger (D^\mu \phi) - \mu^2 \phi^\dagger \phi - \frac{1}{2} \lambda (\phi^\dagger \phi)^2 \quad (2.11)$$

4. \mathcal{L}_Y - Yukawa Interactions part that describes the interaction of fermions with the Higgs field, leading to the generation of fermion masses after spontaneous symmetry breaking. These interactions are known as Yukawa interactions. Finally, the Yukawa Lagrangian \mathcal{L}_Y is expressed as:

$$\mathcal{L}_Y = Y_N^1 e_N \bar{l}_N \phi + Y_N^2 d_N \bar{q}_N \phi + Y_{NM}^3 u_M \bar{q}_N \hat{\phi} + \text{h.c.} \quad (2.12)$$

Using $\hat{\phi} = i\sigma_2 \phi$, we performed rotations in the family space to diagonalize as many Yukawa matrices Y^i as feasible, while maintaining the invariance of the remaining Lagrangian components. Specifically, an additional rotation of u permits us to establish Y_{NM}^3 as a unitary matrix multiplied by a diagonal matrix, $Y_{NM}^3 \equiv Y_M^3 V_{NM}^\dagger$, without any loss of generality.

In Eqs. 2.4 and 2.7, both fermions and gauge bosons are treated as massless. However, after spontaneous symmetry breaking (SSB), these particles acquire mass through the Higgs mechanism, where the Higgs field acquires a non-zero vacuum expectation value (VEV), thereby breaking the initial symmetry of the Standard Model.

2.2 Spontaneous Symmetry Breaking

In Eq. 2.11, \mathcal{L}_S represents the Lagrangian of the complex ϕ^4 theory. This theory maintains invariance under the global U(1) symmetry transformation:

$$\phi(x) \rightarrow e^{i\alpha} \phi(x) \quad (2.13)$$

where α is a global parameter. In a theory without symmetry breaking, the Lagrangian includes a positive mass term ($\mu^2 > 0$), leading to a potential $V =$

$\mu^2\phi^\dagger\phi + \frac{1}{2}\lambda(\phi^\dagger\phi)^2$, which forms a parabolic shape (Fig:2.1a). There exists a unique symmetric vacuum state where perturbations are symmetric under U(1) phase rotations [1].

For spontaneous symmetry breaking, the mass term is negative ($\mu^2 < 0$). The potential then resembles a Mexican hat shape (Fig:2.1b), with a local maximum at $\phi = 0$ that is unstable. The field condenses into one of many degenerate vacuum states lying on a ring in the complex plane (red ring in the figure).

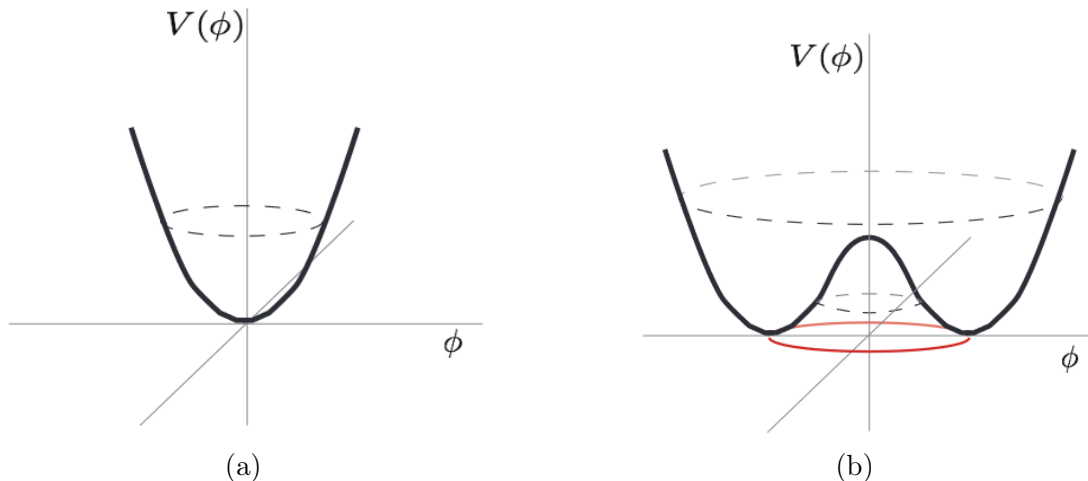


Figure 2.1: (a) $\mu^2 > 0$: the ground state is uniquely located at $\phi = 0$, maintaining the U(1) symmetry of the Lagrangian (b) $\mu^2 < 0$: the ground state becomes degenerate, with each ground state breaking the U(1) symmetry of the Lagrangian [1].

When the vacuum breaks the gauge symmetry, the electroweak group experiences SSB to the electromagnetic subgroup [19]:

$$SU(3)_C \times SU(2)_L \times U(1)_Y \xrightarrow{\text{SSB}} SU(3)_C \times U(1)_{\text{QED}} \quad (2.14)$$

The mechanism of SSB is responsible for the generation of weak gauge boson masses. It leads to the emergence of a physical scalar particle within the model known as the Higgs boson. A final essential component is required to construct the Standard Model. If μ^2 is less than zero and λ is greater than zero in \mathcal{L}_S , the potential exhibits a degenerate minimum at $|\langle\phi\rangle| = \frac{v}{\sqrt{2}} \equiv \sqrt{\frac{-2\mu^2}{\lambda}}$. The mechanism of SSB also gives rise to fermion masses and mixings. Within the SM framework, the symmetry $SU(2)_L \times U(1)_Y$ is spontaneously broken down to $U(1)_{em}$ by selecting

$$\langle\phi\rangle = 2^{-\frac{1}{2}} \begin{pmatrix} 0 \\ v \end{pmatrix} \quad (2.15)$$

between them. The symbol v represents the VEV of the Higgs field in SM. The value of v is approximately 246 GeV [20]. To account for perturbations around the minimum, we parameterize the field $\phi(x)$ as:

$$\phi(x) = \frac{e^{i\sigma_i\theta_i(x)/2}}{\sqrt{2}} \begin{pmatrix} 0 \\ v + H(x) \end{pmatrix} \quad (2.16)$$

By choosing a local $SU(2)_L$ gauge transformation for $\phi(x)$, the term involving $\theta(x)$ can be completely vanished from the Lagrangian, resulting in a new scalar boson $H(x)$.

Before symmetry breaking, the gauge bosons associated with the $SU(2)_L$ group were massless. These bosons acquire mass by interacting with the scalar field ϕ via the covariant derivative. The charged gauge bosons $W_\mu^\mp \equiv W_\mu^1 \pm iW_\mu^2/\sqrt{2}$ are already diagonalized, whereas the massless photon A_μ and the massive Z_μ boson result from the diagonalization of the mass matrix formed by $W_3^\mu - B_\mu$.

Similarly, fermions obtain their masses via the Yukawa Lagrangian. Upon expanding the mass component of Eq. (2.12), we find:

$$\mathcal{L}_Y = \frac{v}{\sqrt{2}} \left(Y_N^1 \bar{d}_{LN} d_{RN} + Y_N^2 \bar{e}_{LN} e_{RN} + Y_M^3 V_{NM}^\dagger \bar{u}_{LN} u_{RM} \right) + \text{h.c.} \quad (2.17)$$

To express the Lagrangian in physical field terms, an additional transformation is necessary to diagonalize the final mass matrix, indicated as $u_{LN} \rightarrow V_{NM}^\dagger u_{LM}$. This transformation only affects the non-diagonal component of the covariant derivative in $iq^{(1)} \not{D} q^{(1)}$ Eq. (2.4). This expression, alongside its leptonic counterpart, corresponds to the charged current Lagrangian \mathcal{L}_{CC} , which holds significant importance in this thesis, particularly in the context of τ decays. It is represented by:

$$\mathcal{L}_{CC} = -\frac{g}{\sqrt{2}} W_\mu^\dagger \left(V_{NM}^\dagger \bar{u}_{LN} \gamma^\mu d_{LM} + \bar{\nu}_{LN} \gamma^\mu e_{LN} \right) + \text{h.c.} \quad (2.18)$$

2.3 Hadronic Decay Modes of the τ Lepton

The decay of the τ lepton into hadrons involves contribution from both terms of Eq. (2.18). To determine the matrix element for this process, we use the Dyson series expansion of the S-matrix, with \mathcal{L}_{CC} as the key component of the interaction Lagrangian. The challenge arises from the fact that final hadronic states $\langle f |$ are produced by quark currents, as these are not elementary particles in high-energy theory. This leads to a matrix element dependent on the non-trivial hadronic component:

$$\mathcal{M}_{\tau \rightarrow f \nu_\tau} = -\frac{g^2 V_{uD}^\dagger}{2} \frac{1}{q^2 - M_W^2} \bar{\nu}_L \gamma^\mu \tau_L \langle f(p_f) | \mathcal{J}_\mu^{Du}(0) | 0 \rangle \quad (2.19)$$

here, $\mathcal{J}_\mu^{Du} = \bar{D}_L \gamma_\mu u_L$, $q = p_\tau - p_{\nu_\tau}$, and $D = s$ or d . Since:

$$s = q^2 = m_\tau^2 - 2m_\tau |\vec{p}_{\nu_\tau}|$$

and knowing that:

$$s < m_\tau^2 \ll M_W^2,$$

q^2 is much smaller than M_W^2 ($q^2 \ll M_W^2$), we can approximate q^2 as being negligible compared to M_W^2 :

$$q^2 - M_W^2 \approx -M_W^2$$

Therefore:

$$\frac{1}{q^2 - M_W^2} \approx \frac{1}{-M_W^2} = -\frac{1}{M_W^2}$$

Now Eq: 2.19 becomes:

$$\mathcal{M}_{\tau \rightarrow f \nu_\tau} = \frac{g^2 V_{uD}^\dagger}{2M_W^2} \bar{\nu}_L \gamma^\mu \tau_L \langle f | \mathcal{J}_\mu^{Du}(0) | 0 \rangle \quad (2.20)$$

This result is equivalent to the one obtained using Fermi's theory:

$$\mathcal{L}_{CC} = -2\sqrt{2}G_F (\bar{d}_{LN} V_{NM}^\dagger \gamma^\mu u_{LM}) (\bar{\nu}_{LN} \gamma_\mu e_{LN}) + \text{h.c.} \quad (2.21)$$

The expression for the hadronic-invariant mass distribution $d\Gamma(s)$ for a final state $\langle f \nu_\tau |$ is given by [21]:

$$d\Gamma(s) = G_F^2 |V_{ud}|^2 S_{EW} \frac{m_\tau^5}{4\pi} \frac{ds}{m_\tau^2} \left(1 - \frac{s}{m_\tau^2}\right)^2 \left\{ \left(1 + \frac{2s}{m_\tau^2}\right) H^{(1)}(s) + H^{(0)}(s) \right\} \quad (2.22)$$

$H^{(i)}$ is defined as follows:

$$H_{\mu\nu}(s) = (-g_{\mu\nu}s + q_\mu q_\nu) H^{(1)}(s) + q_\mu q_\nu H^{(0)}(s) \quad (2.23)$$

with

$$H_{\mu\nu} \equiv (2\pi)^3 \int d\Phi_f \delta^4(p_f - q) \langle n | \mathcal{J}_\mu^{Du}(0) | 0 \rangle \langle 0 | \mathcal{J}_\nu^{Du\dagger}(0) | f \rangle \quad (2.24)$$

where Φ_f is the phase space of the f final hadrons, and p_f is the total momentum. τ lepton can decay into various final states, including single-hadron and two-hadron final states.

2.3.1 Single Hadron Decays

For single hadron decays, we consider the general process:

- $\tau^- \rightarrow H^- \nu_\tau$

where H is hadron. The hadronic matrix element for this process, which involves the weak current responsible for the transition, is given by:

$$\langle H^- | \mathcal{J}_\mu^{Du} | 0 \rangle = i f_H p_\mu^H \quad (2.25)$$

where:

- f_H is the decay constant for hadron,
- p_μ^H is the four-momentum of the hadron.

The decay width is generally expressed as [22]:

$$\Gamma(\tau^- \rightarrow H^- \nu_\tau) = \frac{G_F^2 |V_{uD}|^2 f_H^2 m_\tau^3}{16\pi} \left(1 - \frac{m_H^2}{m_\tau^2}\right)^2 \quad (2.26)$$

2.3.2 Two Hadron Decays

For two hadron decays, we consider the following general process:

- $\tau^- \rightarrow H^- H'^{(0)} \nu_\tau$

For two final hadrons H^- and $H'^{(0)}$, the hadronic matrix element has two possible Lorentz structures:

$$\begin{aligned} \langle H^-(p) H'^{(0)}(p') | \mathcal{J}_\mu^{Du} | 0 \rangle = \frac{c_{HH^0}}{2} \left\{ \left(P^- - \frac{\Delta_{HH^0}}{s} P^+ \right)_\mu F_+^{HH^0}(s) \right. \\ \left. + \frac{\Delta_{HH^0}}{P^+} P_\mu^- F_S^{HH^0}(s) \right\} \end{aligned} \quad (2.27)$$

where $F_+^{HH^0}(s)$, $F_S^{HH^0}$ are the vector and scalar form factors respectively, $\Delta_{HH^0} = m_H^2 - m_{H^0}^2$, $P^+ \equiv p + p^0$, $P^- \equiv p - p^0$, and $s = P^{+2}$. The normalization coefficients c_{HH^0} are [21]:

$$c_{\pi\pi} = \sqrt{2}, \quad c_{K\bar{K}} = -1, \quad c_{K\pi} = \frac{1}{\sqrt{2}}, \quad c_{\pi\bar{K}} = -1, \quad c_{\pi\eta'} = -\sqrt{2} \quad (2.28)$$

The Lorentz structures correspond to $J = 1$ and $J = 0$, as per Eq. (2.24):

$$H^{(1)}(s) = (2\pi)^3 \frac{c_{HH^0}^2}{12s^2} \lambda(s, m_H^2, m_{H^0}^2) |F_+^{HH^0}(s)|^2 \int d\Phi_2 \delta^4(s - P^{+2}) \quad (2.29)$$

and

$$H^{(0)}(s) = (2\pi)^3 \frac{c_{HH^0}^2}{4s^2} |F_S^{HH^0}(s)|^2 \int d\Phi_2 \delta^4(s - P^{+2}) \quad (2.30)$$

Using:

$$\int d\Phi_2 \delta^4(s - P^{+2}) = \frac{\pi \lambda^{1/2}(s, m_H^2, m_{H^0}^2)}{(2\pi)^6 s} \quad (2.31)$$

we get [18]:

$$\begin{aligned} \frac{d\Gamma_{\tau \rightarrow H^- H'^{(0)} \nu_\tau}}{ds} = & G_F^2 |V_{uD}|^2 \frac{m_\tau^3 S_{EW}}{768 \pi^3 s^3} c_{HH^0}^2 \left(1 - \frac{s}{m_\tau^2}\right)^2 \\ & \times \left\{ \left(1 + 2 \frac{s}{m_\tau^2}\right) \lambda^{3/2}(s, m_H^2, m_{H^0}^2) |F_+^{HH^0}(s)|^2 \right. \\ & \left. + 3 \Delta_{HH^0}^2 \lambda^{1/2}(s, m_H^2, m_{H^0}^2) |F_S^{HH^0}(s)|^2 \right\} \end{aligned} \quad (2.32)$$

In this thesis, we will consider these two hadron decays and to study these decays we will use the framework of Effective Field Theory (EFT).

2.4 Effective Field Theory

EFT is a successful approach in quantum field theory (QFT) because it offers a formalism for systematically investigating problems that involve multiple scales. This holds particular significance in QCD, where the running coupling, $\alpha_s(\mu)$, varies considerably across different energy scales. This theory simplifies practical computations in QFT. It also offers a modern understanding of “renormalization”.

The core concept of EFT is expressed as follows: We examine the QFT, particularly focusing on a fundamental scale M , which denotes the mass or significant momentum transfer associated with a heavy particle [23]. Suppose our interest lies in studying physics occurring at significantly lower energies E as well as momenta p compared to M . What is the method for decomposing the decay or scattering amplitudes into a series of E/M powers? Addressing this question involves a few steps:

1. Select a cutoff Λ that is less than M , then separate the theory’s fields into two categories: low- and high-frequency modes,

$$\phi = \phi_L + \phi_H \quad (2.33)$$

In this division, the low-frequency modes, consisting of Fourier modes with frequencies $\omega < \Lambda$ are contained in ϕ_L , while the other modes with frequencies $\omega > \Lambda$ are contained in ϕ_H .

The cutoff may be thought of as a “threshold of ignorance”, implying we disregard any knowledge regarding the theory at scales beyond Λ . The ϕ_L fields characterize the physics at low energy. The vacuum correlation functions of these fields can provide all of the information needed for the theory, including Feynman diagrams, cross sections, scattering amplitudes, and decay rates. One can determine these correlators by using:

$$\langle 0|T\{\phi_L(x_1)\dots\phi_L(x_n)\}|0\rangle = \frac{1}{Z[0]} \frac{\delta}{\delta J_L(x_1)} \dots \frac{\delta}{\delta J_L(x_n)} Z[J_L] \Big|_{J_L=0} \quad (2.34)$$

here

$$Z[J_L] = Z \int \mathcal{D}\phi_H \mathcal{D}\phi_L e^{iS(\phi_H, \phi_L) + i \int d^D x J_L(x) \phi_L(x)} \quad (2.35)$$

This expression represents the generating functional, where D is the space-time dimension, $S(\phi_H, \phi_L) = \int d^D x \mathcal{L}$ represents the action, and sources J_L have been introduced for light fields.

2. Furthermore, we evaluate the path integral for high-frequency fields, yielding

$$Z[J_L] = \int \mathcal{D}\phi_L e^{iS_\Lambda(\phi_L) + i \int d^D x J_L(x) \phi_L(x)} \quad (2.36)$$

where

$$e^{iS_\Lambda(\phi_L)} = \int \mathcal{D}\phi_H e^{iS(\phi_H, \phi_L)} \quad (2.37)$$

is known as the “Wilsonian effective action”. The selection of the cutoff Λ among low- and high-frequency modes affects this action. On scales $\Delta x \sim 1/\Lambda$, the action S_Λ becomes non-local because the high-frequency fluctuations are excluded from this theory. The method of excluding such modes is commonly known as “integrating out” the high-frequency fields in a functional integral.

3. Finally, we expand the non-local action to include local operators made up of low-energy fields. This procedure is known as “Operator-Product Expansion”, where two operators $\hat{O}_1(x)\hat{O}_2(y)$ are expanded as:

$$\hat{O}_1(x)\hat{O}_2(y) = \sum_i c_i(x, y) Q_i(y) \quad (2.38)$$

Coefficients $c_i(x, y)$ scale as $\frac{c_i}{(x-y)^{d_{O_1} + d_{O_2} - d_{Q_i}}}$, where d_{Q_i} represents the scaling dimension of the operator Q_i , which may undergo modifications known as anomalous dimensions due to quantum corrections. As y approaches x , operators with lower dimensions tend to dominate the summation. This OPE

works under the assumption that $E \ll \Lambda$. The outcome may be represented as follows:

$$S_\Lambda(\phi_L) = \int d^D x \mathcal{L}_{\text{eff}}^\Lambda(x) \quad (2.39)$$

where

$$\mathcal{L}_{\text{eff}}^\Lambda(x) = \sum_i \alpha_i Q_i(\phi_L(x)) \quad (2.40)$$

This is known as the “effective Lagrangian”. It consists of an infinite series of local operators Q_i multiplied by coupling constants α_i , known as Wilson coefficients. Generally, this sum includes all operators permitted by the theory’s symmetries that are formed during the formation of the effective Lagrangian.

The Wilson coefficients α_i are obtained from the renormalization group equation [18]:

$$\left(\mu \frac{d}{d\mu} - \gamma_{Q_i} \right) \alpha_i = 0 \quad (2.41)$$

In this equation:

- $\mu \frac{d}{d\mu}$ represents the derivative with respect to the renormalization scale μ , indicating how the Wilson coefficients evolve as the scale changes.
- γ_{Q_i} is the anomalous dimension of the operator Q_i . It quantifies the scaling behavior of the operator due to quantum corrections.

Several important factors must be considered while constructing the leading terms of the effective weak Lagrangian. Firstly, it’s crucial to recognize that four fermion fields inherently possess dimension $\delta_i = 6$, implying that no additional fields or derivatives are permissible in this order. Moreover, weak interactions involve fermion fields that are exclusively left-handed. Additionally, in strong-interaction processes, chirality remains conserved, allowing us to set $m_q = 0$ at the leading power. The only permissible choice for Γ from the Dirac basis, in the context of quark bilinears $\bar{\psi}_L \Gamma \psi_L$, is $\Gamma = \gamma^\mu$. Lastly, operators have to be Lorentz invariant and gauge invariant, especially color singlets.

Let’s provide an example to better understand EFT. Semileptonic decays, like $\bar{B}^0 \rightarrow \pi^+ e^- \bar{\nu}_e$, arise from the quark transition $b \rightarrow u e^- \bar{\nu}_e$. The above-mentioned factors can be used to determine the CKM matrix element $|V_{ub}|$. The relevant effective Lagrangian includes a unique dimension-6 operator, $\bar{e}_L \gamma^\mu \nu_L \bar{u}_L \gamma_\mu b_L^i$. The W boson in Figure 2.2 is integrated out to get this operator. In the following, we will skip color indices i that are contracted across adjacent quark fields. The outcome of the tree-level matching is as follows:

$$\mathcal{L}_{\text{eff}} = -\frac{4G_F}{\sqrt{2}} V_{ub} C_1(\mu) \bar{e}_L \gamma^\mu \nu_L \bar{u}_L \gamma_\mu b_L \quad (2.42)$$

with $C_1 = 1 + \mathcal{O}(\alpha_s)$ and G_F here is the Fermi constant which is related to the mass of W boson and coupling strength g of the weak interaction, associated with the W boson: $G_F \sim \frac{g^2}{M_W^2} \sim 10^{-5} \text{ GeV}^{-2}$.

In the SM, weak interactions occur via the exchange of W bosons. Only the interactions between weak charged gauge bosons W^\pm and fermions result in flavor-changing currents in the SM. The heavy bosons from the SM Lagrangian may be integrated out when examining the weak interaction at low energy scales in EFT, as Figure 2.2 illustrates.

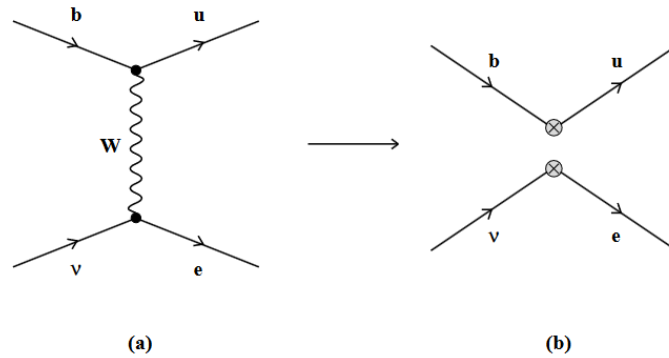


Figure 2.2: (a) In the Standard Model, integrating out the W boson yields an effective four-fermion interaction. (b) The two crossed circles indicate a local four-quark operator within the EFT [2]

Chapter 3

Investigating τ Decays using Effective Field Theory

This chapter provides a brief overview of Effective Field Theory (EFT), Chiral symmetry, Chiral Perturbation Theory (ChPT), and Resonance Chiral Theory (RChT). Firstly, we will write the low-energy charged current Lagrangian governing these decays. Subsequently, we discuss the Chiral Perturbation Theory, which is utilized to study the form factors for these decays. A thorough examination of these form factors will be provided in Chapter 4.

3.1 Effective Field Theory as a Tool to Investigate τ Decays

We have specifically considered semileptonic τ decays in our work and used the EFT framework to accommodate potential new physics effects, emphasizing a model-independent approach.

Being the heaviest of the charged leptons, the τ lepton occupies a unique position in the SM of particle physics. Several factors motivate the detailed study of τ decays:

- τ leptons can decay both leptonically (into lighter leptons and neutrinos) and hadronically (into hadrons and its neutrino). This diversity allows for the study of both weak and strong interactions within a single framework.
- Due to its high mass and complex decay modes, the τ lepton is sensitive to various potential new physics scenarios, including supersymmetry, leptoquarks, and other extensions of the SM. Any deviations from SM predictions in τ decays could provide indirect evidence for new physics.

EFT offers a systematic method to explore the interactions involved in τ decays by expanding the Lagrangian in terms of operators with increasing dimensions:

Standard Model Effective Field Theory (SMEFT): At energies below the electroweak scale, the SMEFT framework allows us to include higher-dimensional operators that encapsulate the effects of new physics. These operators are suppressed by the scale of new physics, making their contributions small but potentially observable in precise measurements.

Low-Energy Effective Theories: At energy scales relevant to τ decays, effective theories such as ChPT and RChT can be employed to describe hadronic interactions. These theories incorporate the symmetries of the strong interaction and are particularly useful for modeling the hadronic decay modes of the tau.

Non-perturbative Techniques: Given the non-perturbative nature of QCD at low energies, lattice QCD and other non-perturbative methods are crucial for calculating the hadronic matrix elements that enter the decay amplitudes.

3.2 The Framework of Effective Field Theory

At the weak scale, the effective Lagrangian incorporates six-dimensional operators that are invariant under $SU(2)_L \otimes U(1)$, contributing to low-energy charged current processes, is expressed as [24, 25]:

$$\mathcal{L}_{\text{eff}} = \mathcal{L}_{\text{SM}} + \frac{1}{\Lambda^2} \sum_i \alpha_i O_i \rightarrow \frac{1}{v^2} \sum_i \hat{\alpha}_i O_i \quad (3.1)$$

here, Λ is the energy scale associated with NP (typically around 1 TeV), α_i are the couplings of the dimension-six operators O_i at the scale Λ with $\hat{\alpha}_i = \frac{v^2}{\Lambda^2} \alpha_i$ denoting the dimensionless couplings of NP, which typically range around 10^{-3} for a scale of approximately 1 TeV. Approximately, $\frac{v^2}{\Lambda^2}$ is about 0.06. Therefore, $\hat{\alpha}_i \approx 0.06 \times \alpha_i$.

For semi-leptonic transitions ($\ell = e, \mu, \tau$) containing only left-handed neutrino fields, the effective Lagrangian at low scales ($O(1 \text{ GeV})$) is expressed as follows:

$$\begin{aligned} \mathcal{L}_{CC} = & -\frac{4G_F}{\sqrt{2}} V_{ud} \left[(1 + [g_v^L]_{\ell\ell}) \bar{\ell}_L \gamma_\mu \nu_{\ell L} \bar{u}_L \gamma^\mu d_L \right. \\ & + [g_v^R]_{\ell\ell} \bar{\ell}_L \gamma_\mu \nu_{\ell L} \bar{u}_R \gamma^\mu d_R + [g_s^L]_{\ell\ell} \bar{\ell}_R \nu_{\ell L} \bar{u}_R d_L + [g_s^R]_{\ell\ell} \bar{\ell}_R \nu_{\ell L} \bar{u}_L d_R \\ & \left. + [g_t^L]_{\ell\ell} \bar{\ell}_R \sigma_{\mu\nu} \nu_{\ell L} \bar{u}_R \sigma^{\mu\nu} d_L \right] + \text{h.c.} \end{aligned} \quad (3.2)$$

Here, g_v^L and g_v^R are associated with vector couplings for leptons, g_s^L and g_s^R represents the scalar couplings for leptons, and g_t^L is associated with tensor couplings. Subscripts $L(R)$ indicate chiral projections that are left- or right-handed

and $\sigma^{\mu\nu} \equiv i[\gamma^\mu, \gamma^\nu]/2$.

In eq: (3.2), setting $g_v^L = g_v^R = g_s^L = g_s^R = g_t^L = 0$ represents the Standard Model Lagrangian. In this expression, all the heavy degrees of freedom are integrated out. The effective couplings $g_v^L, g_v^R, g_s^L, g_s^R, g_t^L$ characterizing New Physics are assumed to be real since we focus on CP-even observables (observable remains invariant under a CP transformation).

In terms of equivalent effective couplings $\epsilon_{L,R} = g_v^{L,R}$, $\epsilon_S = g_s^L + g_s^R$, $\epsilon_P = g_s^L - g_s^R$, and $\epsilon_T = g_t^L$, the effective Lagrangian, specific to $\ell = \tau$, takes the following form ¹:

$$\begin{aligned} \mathcal{L}_{CC} = & -\frac{G_F V_{ud}(1 + \epsilon_L + \epsilon_R)}{\sqrt{2}} \left[\bar{\tau} \gamma_\mu (1 - \gamma_5) \nu_\tau \cdot \bar{u} (\gamma^\mu - (1 - 2\hat{\epsilon}_R) \gamma^\mu \gamma_5) d \right. \\ & \left. + \bar{\tau} (1 - \gamma_5) \nu_\tau \cdot \bar{u} (\hat{\epsilon}_S - \hat{\epsilon}_P \gamma_5) d + 2\hat{\epsilon}_T \bar{\tau} \sigma_{\mu\nu} (1 - \gamma_5) \nu_\tau \cdot \bar{u} \sigma^{\mu\nu} d \right] + \text{h.c.} \quad (3.3) \end{aligned}$$

here $\hat{\epsilon}_i \equiv \epsilon_i / (1 + \epsilon_L + \epsilon_R)$ for $i = R, S, P, T$. This factorized form is useful when appropriately normalized rates allow the cancellation of the overall factor $(1 + \epsilon_L + \epsilon_R)$. The expressions for the $\hat{\epsilon}_i$ are obtained by retaining terms linear in small effective couplings, reducing them to the form given in [24].

3.3 Chiral Symmetry

Consider N_f flavors of massless quarks represented in flavor space by the vector field: $\psi^A = (u, d, \dots)$. The corresponding QCD Lagrangian is:

$$\mathcal{L}_0 = -\frac{1}{4} G_{\mu\nu}^a G_a^{\mu\nu} + i\bar{\psi}_L \gamma^\mu D_\mu \psi_L + i\bar{\psi}_R \gamma^\mu D_\mu \psi_R \quad (3.4)$$

where the gluon interactions are encoded in the flavor-independent covariant derivative D_μ . The form of the covariant derivative D_μ , which acts on the quark fields ψ_L and ψ_R , can be expressed as:

$$D_\mu = \partial_\mu - ig_s G_\mu^a \frac{\lambda^a}{2} \quad (3.5)$$

Without a quark mass term, interactions between left- and right-handed quark chiralities occur only through gluon interactions. The QCD Lagrangian remains

¹Physical amplitudes in particle physics are independent of the renormalization scale [26]. However, effective couplings ϵ_i and hadronic matrix elements are scale-dependent. Conventionally, $\mu = 2$ GeV is chosen in the MS scheme.

invariant under global transformations $G \equiv SU(N_f)_L \times SU(N_f)_R$ that act independently on the left and right chiral quark fields:

$$\psi_L \xrightarrow{G} g_L \psi_L, \quad \psi_R \xrightarrow{G} g_R \psi_R, \quad g_{L,R} \in SU(N_f)_{L,R}. \quad (3.6)$$

The Noether currents associated with chiral group G are expressed as:

$$J_X^{i\mu} = \bar{\psi}_X \gamma^\mu T^i \psi_X, \quad (X = L, R; i = 1, \dots, N_f^2 - 1) \quad (3.7)$$

with T^i being the $SU(N_f)$ generators. The Noether charges Q_X^i associated with these currents obey the following commutation relations:

$$[Q_X^i, Q_Y^j] = i\delta_{XY} f^{ijk} Q_X^k \quad (3.8)$$

involving the $SU(N_f)$ structure constants f^{ijk} . These algebraic relations formed the foundation of current algebra techniques before the development of QCD.

The hadronic spectrum in the light quark sector (u, d, s) does not exhibit chiral symmetry as described by Eq.(3.6). A Wigner–Weyl realization would predict degenerate mirror multiplets with opposite chiralities, but such multiplets are not observed. The fact that the octet of pseudoscalar mesons is lighter than other hadronic states indicates that the vacuum does not exhibit symmetry under the complete chiral group. Only transformations where $g_R = g_L$ preserve symmetry, leading to the breakdown of $SU(3)_L \times SU(3)_R$ symmetry to $SU(3)_{L+R}$.

The eight broken axial generators $Q_A^a = Q_R^a - Q_L^a$ correspond to eight pseudoscalar Nambu-Goldstone bosons ($\pi^-, \pi^+, \pi^0, \eta, K^-, K^+, K^0, \bar{K}^0$). The small masses of these particles arise from the quark-mass matrix, which breaks the global chiral symmetry of the QCD Lagrangian. The quark condensate:

$$\langle 0 | \bar{q}q | 0 \rangle \neq 0 \quad (3.9)$$

is the natural order parameter of dynamical chiral symmetry breaking (χ_{SB}). For $N_f = 2$, $\psi^A = (u, d)$, the pattern of χ_{SB} predicts three Nambu-Goldstone bosons, which are the pion multiplet [27].

3.3.1 Formulating the Chiral Lagrangian in QCD

The matrix element of a transformation is written as [28]:

$$g = \begin{pmatrix} L & 0 \\ 0 & R \end{pmatrix} \quad (3.10)$$

where $L(R)(x) = e^{i\lambda_i \theta_i}$ and λ_i are the $SU(3)$ generators. Due to the Goldstone Theorem, each generator of the unbroken symmetry has an associated Goldstone

boson. At low energies, these are the primary degrees of freedom.

To parametrize these fields, we apply the CCWZ formalism². By assuming that a local field configuration represents an excitation of the vacuum ϕ_0 , such that $\phi(x) = \Theta(x)\phi_0$, where $\Theta(x)$ is an element of $SU(3)_L \times SU(3)_R$, we can express it as:

$$\Theta(x) = \begin{pmatrix} 1 & 0 \\ 0 & U(x) \end{pmatrix} \begin{pmatrix} V(x) & 0 \\ 0 & V(x) \end{pmatrix} \quad (3.11)$$

Since ϕ_0 remains invariant under any local $SU(3)_V$ ($L = R$) transformation, therefore we may select any $V(x)$ without modifying the configuration. Choosing $V(x) = I$, all configurations are parametrized by the local transformation of the right generators,

$$U(x) = e^{i\lambda_i \frac{\phi_i(x)}{F}} \quad (3.12)$$

where λ_i represents a Gell-Mann matrix, and F is a dimensional parameter introduced to balance the dimensions of ϕ_i . For a global group transformation g , as previously defined in Eq. (3.10):

$$\phi(x) \rightarrow g\phi(x) \implies \Theta(x) \rightarrow g\Theta(x) \quad (3.13)$$

generally:

$$g\Theta(x) = \begin{pmatrix} 1 & 0 \\ 0 & RU(x)L^\dagger \end{pmatrix} \begin{pmatrix} L & 0 \\ 0 & L \end{pmatrix} \neq \begin{pmatrix} 1 & 0 \\ 0 & U_1 \end{pmatrix} \quad (3.14)$$

We can choose that after the transformation, the matrix $\Theta(x)$ becomes:

$$\Theta(x) \rightarrow \Theta'(x) = g\Theta(x) \begin{pmatrix} V(x) & 0 \\ 0 & V(x) \end{pmatrix} \quad (3.15)$$

with an arbitrary $V(x)$. By selecting $V(x) = L^\dagger$, the resulting transformed $\Theta'(x)$ can be parameterized once more using the local transformation linked with the right generators:

$$U(x) = e^{i\lambda_i \frac{\phi_i(x)}{F}} \quad \text{with} \quad U(x) \rightarrow RU(x)L^\dagger \quad (3.16)$$

The dimensional quantity F identifies the fields $\phi(x)$ as spin-0 bosons. We now construct the most general Lagrangian that preserves the symmetries for $U(x)$, which encapsulates the low-energy degrees of freedom. By imposing invariance under $SU(3)_L \times SU(3)_R$ transformations, and noting that $U(x) \rightarrow RU(x)L^\dagger$, we find that the invariant quantities are the flavor traces of $U(x)$ and $U^\dagger(x)$.

$$\mathcal{L}_{\text{LO}} = \frac{F^2}{4} \text{Tr}(\partial^\mu U(x) \partial_\mu U(x)) \quad (3.17)$$

²Callan, Coleman, Wess, and Zumino developed the general formalism for Effective Lagrangian involving spontaneously broken symmetries.

The prefactor is fixed by requiring proper normalization of the kinetic term for Goldstone bosons when expanding $U(x)$. The higher-order corrections arise from loop contributions and are given by:

$$\text{Loop} \sim \left(\frac{E}{4\pi F} \right)^2 \text{Tree} \quad (3.18)$$

where E represents the energies involved in the process. This counting is valid as long as $E \ll 4\pi F$. Loop divergences are canceled by renormalizing the low energy constants of higher-order Lagrangians, encoding short-distance information obtainable from lattice QCD or estimated analytically, such as through Resonance Chiral Theory with additional assumptions. Alternatively, these constants can be fixed using experimental data, though this approach costs of losing some predictive power, but their natural order matches loop corrections [18].

3.4 Chiral Perturbation Theory (ChPT)

ChPT is an effective field theory based on the spontaneous breaking of chiral symmetry observed in QCD. It provides a systematic framework to describe the low-energy interactions of pions and other light mesons. ChPT is organized as an expansion in terms of small momenta and meson masses, respecting the symmetries of QCD. It has been successful in predicting and interpreting experimental data in low-energy hadron physics [29, 30].

In an ideal scenario, massless Nambu–Goldstone bosons arise from exact symmetry. However, physical pions have masses due to explicit χ_{SB} from quark masses and electroweak interactions. To incorporate these effects, we introduce external classical fields that interact with quark currents.

3.4.1 Extended QCD Lagrangian

Consider the extended QCD Lagrangian where quark currents are coupled to external Hermitian matrix-valued fields v_μ , a_μ , s , p . The Lagrangian is expressed as:

$$\mathcal{L}_{\text{QCD}} = \mathcal{L}_0 + \bar{q}\gamma^\mu v_\mu q + \bar{q}\gamma^\mu \gamma_5 a_\mu q - \bar{q}(s - i\gamma_5 p)q \quad (3.19)$$

here, \mathcal{L}_0 represents the massless QCD Lagrangian. These external fields parameterize chiral symmetry breaking:

$$r_\mu \equiv v_\mu + a_\mu, \quad l_\mu \equiv v_\mu - a_\mu, \quad s = M', \quad p = 0. \quad (3.20)$$

In this context, the external fields are related to the gauge fields A_μ by:

$$r_\mu = -eQA_\mu \quad (3.21)$$

$$l_\mu = -eQA_\mu - e\sqrt{2}\sin\theta_W(W_\mu^\dagger A^+ + \text{h.c.}) \quad (3.22)$$

with M' and Q being the quark mass and charge matrices respectively:

$$M' = \text{diag}(m_u, m_d, m_s), \quad Q = \frac{1}{3}\text{diag}(2, -1, -1) \quad (3.23)$$

Here, v_μ includes electromagnetic interactions, s accounts for quark masses, and l_μ incorporates the charged-current couplings of W^\pm bosons, with the matrix A^+ :

$$A^+ = \begin{pmatrix} 0 & V_{ud} & V_{us} \\ 0 & 0 & 0 \\ 0 & 0 & 0 \end{pmatrix} \quad (3.24)$$

3.4.2 Chiral Symmetry Transformations and Effective Lagrangian

The Lagrangian maintains invariance under local $SU(3)_L \times SU(3)_R$ transformations, with external fields transforming as follows:

$$q_R \rightarrow g_R q_R, \quad q_L \rightarrow g_L q_L \quad (3.25)$$

$$s + ip \rightarrow g_R(s + ip)g_L^\dagger \quad (3.26)$$

$$l_\mu \rightarrow g_L l_\mu g_L^\dagger + ig_L \partial_\mu g_L^\dagger \quad (3.27)$$

$$r_\mu \rightarrow g_R r_\mu g_R^\dagger + ig_R \partial_\mu g_R^\dagger \quad (3.28)$$

To ensure local invariance, the gauge fields v_μ and a_μ appear only through covariant derivatives:

$$D_\mu U = (\partial_\mu - ir_\mu)U + iUl_\mu \quad (3.29)$$

$$D_\mu U^\dagger = (\partial_\mu - il_\mu)U^\dagger + iU^\dagger r_\mu \quad (3.30)$$

and through the field strength tensors:

$$F_{\mu\nu}^L = \partial_\mu l_\nu - \partial_\nu l_\mu - i[l_\mu, l_\nu] \quad (3.31)$$

$$F_{\mu\nu}^R = \partial_\mu r_\nu - \partial_\nu r_\mu - i[r_\mu, r_\nu] \quad (3.32)$$

The most general effective Lagrangian, to leading order in terms of derivatives and external fields, is given by:

$$\mathcal{L} = \frac{F^2}{4} \text{Tr}[D_\mu U^\dagger D^\mu U + U^\dagger \chi + \chi^\dagger U] \quad (3.33)$$

with

$$\chi = 2B(s + ip) \quad (3.34)$$

Here, F denotes the pion decay constant, and B refers to the quark vacuum condensate.

3.4.3 Noether Currents and Generating Functional

The generating functional $Z[v, a, s, p]$ relates fundamental and effective theories:

$$e^{iZ} = \int Dq D\bar{q} DG_\mu e^{i \int d^4x \mathcal{L}_{\text{QCD}}} = \int DU e^{i \int d^4x \mathcal{L}_{\text{eff}}} \quad (3.35)$$

with the classical action at the lowest order:

$$S = \int d^4x \mathcal{L} \quad (3.36)$$

The chiral Noether currents are:

$$J_\mu^L = \bar{q}_L \gamma_\mu q_L \stackrel{\cdot}{=} \frac{\delta S}{\delta l_\mu} = \frac{i}{2} F^2 D_\mu U^\dagger U \quad (3.37)$$

$$J_\mu^R = \bar{q}_R \gamma_\mu q_R \stackrel{\cdot}{=} \frac{\delta S}{\delta r_\mu} = \frac{i}{2} F^2 D_\mu U U^\dagger \quad (3.38)$$

The derivatives with respect to the scalar and pseudoscalar sources are given by:

$$\langle \bar{q}_j q_i \rangle = - \frac{\delta S}{\delta (s - ip)_{ji}} = - \frac{F^2}{2} B U_{ji} \quad (3.39)$$

$$\langle \bar{q}_i q_j \rangle = - \frac{\delta S}{\delta (s + ip)_{ji}} = - \frac{F^2}{2} B U_{ji}^\dagger \quad (3.40)$$

$$q_L^j \bar{q}_R^i \stackrel{\cdot}{=} - \frac{\delta S}{\delta (s - ip)_{ji}} = - \frac{F^2}{2} B U_{ij}(\phi) \quad (3.41)$$

$$\bar{q}_R^j q_L^i \stackrel{\cdot}{=} - \frac{\delta S}{\delta (s + ip)_{ji}} = - \frac{F^2}{2} B U_{ij}^\dagger(\phi) \quad (3.42)$$

relating B to the quark vacuum condensate:

$$\langle 0 | \bar{q}_j q_i | 0 \rangle = -F^2 B \delta_{ij} \quad (3.43)$$

The Nambu-Goldstone bosons, parameterized by $U(\phi)$, are zero-energy excitations over the vacuum condensate that cause dynamical chiral symmetry breaking.

3.4.4 Power Counting

ChPT works by expanding the powers of momenta and quark masses, which are treated as small parameters. The effective Lagrangian is structured as follows:

$$\mathcal{L}_{\text{eff}} = \mathcal{L}_{\text{LO}} + \mathcal{L}_{\text{NLO}} + \mathcal{L}_{\text{NNLO}} + \dots, \quad (3.44)$$

where \mathcal{L}_{NLO} and $\mathcal{L}_{\text{NNLO}}$ represent the next-to-leading and next-to-next-to-leading order terms, respectively.

3.5 Resonance Chiral Theory (RChT)

QCD, the theory of the strong interaction, becomes non-perturbative at low energies, making it challenging to describe hadronic processes using quarks and gluons. Effective Field Theories like ChPT are successful in the low-energy regime but are limited to energies significantly below the mass of rho meson M_ρ . RChT extends the description to energies around 1-2 GeV by incorporating resonance and meson fields into a phenomenological Lagrangian framework governed by chiral and unitary symmetries.

3.5.1 Inclusion of Resonances

RChT extends ChPT by explicitly incorporating resonances into the effective field theory framework. Resonances are higher-energy states that couple strongly to pseudo-Goldstone bosons and play a crucial role in processes where intermediate resonant states are significant.

3.5.2 Lagrangian Formulation

The RChT Lagrangian includes both the pseudo-Goldstone bosons and the resonances. For instance, the Lagrangian for vector resonances V_μ is given by:

$$\mathcal{L}_V = -\frac{1}{4}\text{Tr}(V_{\mu\nu}V^{\mu\nu}) + \frac{F_V}{2\sqrt{2}}\text{Tr}(V_{\mu\nu}f_+^{\mu\nu}) \quad (3.45)$$

where $V_{\mu\nu}$ is the field strength tensor of the vector resonance, and $f_+^{\mu\nu}$ contains the field strengths of the external gauge fields [31, 32].

Applications

1. RChT has been successfully applied to study processes such as the $\tau \rightarrow \pi\pi\pi\nu_\tau$ decay. The relevant form factors can be determined using RChT, providing insights into the dynamics of hadron resonances.
2. RChT helps in determining the Low-Energy Constants (LECs) in chiral perturbation theory by matching the effective theory with the resonance region. This establishes a connection between chiral and resonance descriptions.

3.6 Form Factors in τ Decays

Consider the process where a τ lepton decays into three pions. In SM, the decay amplitudes for processes $\tau^- \rightarrow \pi^- \pi^- \pi^+ \nu_\tau$ and $\tau^- \rightarrow \pi^- \pi^0 \pi^0 \nu_\tau$ are given by:

$$\mathcal{M}^\pm = -\frac{G_F V_{ud}}{\sqrt{2}} \bar{u}_{\nu_\tau} \gamma^\mu (1 - \gamma_5) u_\tau T_\mu^\pm \quad (3.46)$$

here, T_μ^\pm represents the hadronic matrix element of the axial-vector QCD current A_μ :

$$T_\mu^\pm(p_1, p_2, p_3) = \langle \pi_1(p_1) \pi_2(p_2) \pi^\pm(p_3) | A_\mu e^{i\mathcal{L}_{\text{QCD}}} | 0 \rangle \quad (3.47)$$

with no contribution from the vector current in the isospin limit. Here, π_1 and π_2 correspond to π^- and π^0 for the upper and lower signs in T_μ^\pm , respectively. The hadronic tensor can be expressed in terms of three form factors, F_1 , F_2 , and F_P as:

$$T_\mu = \left(g_{\mu\nu} - \frac{Q_\mu Q_\nu}{Q^2} \right) (p_1 - p_3)^\nu F_1 + \left(g_{\mu\nu} - \frac{Q_\mu Q_\nu}{Q^2} \right) (p_2 - p_3)^\nu F_2 + Q_\mu F_P \quad (3.48)$$

where $Q_\mu = p_{1\mu} + p_{2\mu} + p_{3\mu}$. Form factors F_1 and F_2 are associated with a $J^P = 1^+$ transition and exhibit a transverse structure in the total hadron momentum Q_μ . The form factor F_P corresponds to a $J^P = 0^-$ transition, representing pseudoscalar degrees of freedom. It vanishes proportionally to the square of the pion mass and thus contributes to the spectral function of $\tau \rightarrow \pi\pi\pi\nu_\tau$ decays at a suppressed level, m_π^4/Q^4 , and is therefore negligible compared to F_1 and F_2 , so it is often disregarded [33].

Form factors F_1 and F_2 can be evaluated in the framework of RChT. The Lagrangian incorporates the original RChT terms and those satisfying OPE of the $\langle VAP \rangle$ Green function³. Additionally, we ensure the smooth asymptotic behavior of the form factors. Various contributions, depicted in diagrams such as Fig. 4.11 and the off-shell widths of $\rho(770)$ and $a_1(1260)$ resonances have also been implemented according to RChT [3].

³The correlation involving vector, axial-vector, and pseudoscalar currents [34]

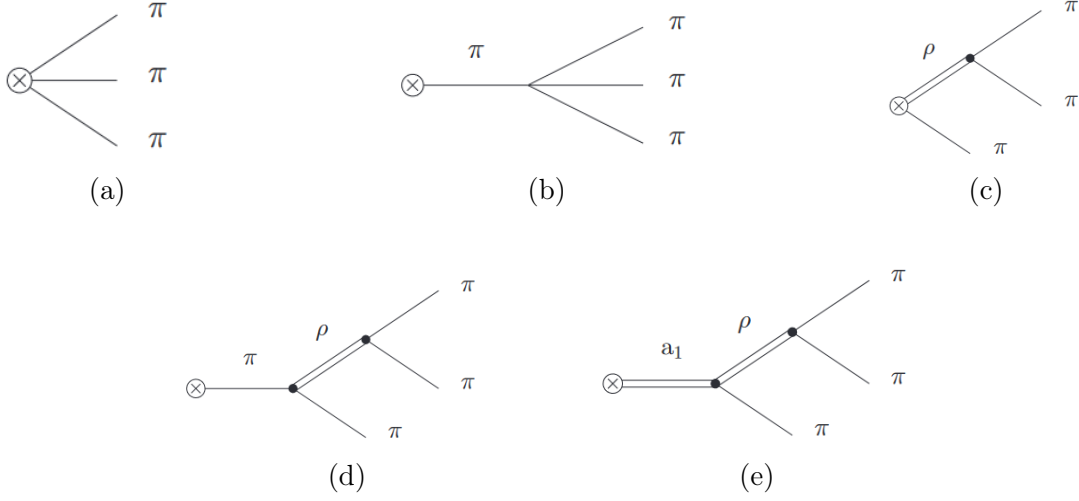


Figure 3.1: The diagrams that contribute to the axial-vector form factors of hadrons [3].

In the decays of $\tau \rightarrow \pi\pi\pi\nu_\tau$, the $\rho(1450)$ resonance, which belongs to a heavier vector nonet, may influence the spectrum. Instead of incorporating an additional nonet in RChT Lagrangian, we modify the ρ Breit-Wigner distribution using an adjustable parameter. Figure 3.2 illustrates a comparison between the ALEPH data [4] and the RChT approach, both with and without the $\rho(1450)$ contribution. The results demonstrate a good agreement with the data when $M_{a_1} \approx 1.120$ GeV.

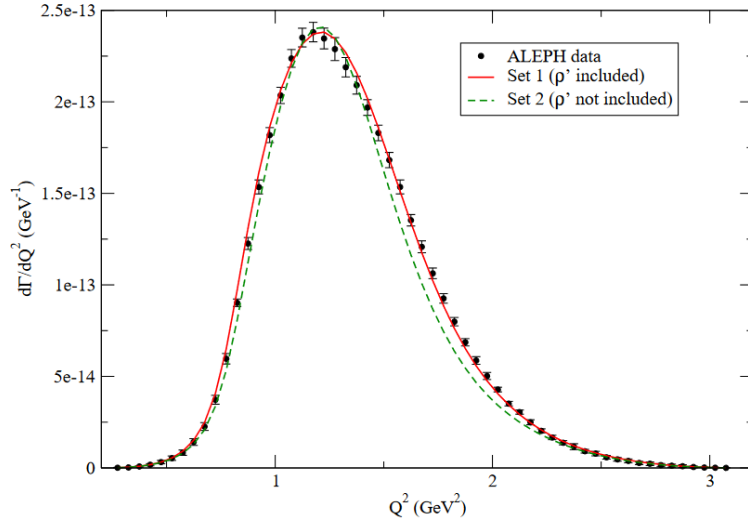


Figure 3.2: Theoretical $M_{\pi\pi\pi}^2$ spectra for the $\tau^- \rightarrow \pi^- \pi^- \pi^+ \nu_\tau$ decay are compared with the experimental results from ALEPH [4].

Chapter 4

Probing New Physics via $\tau^- \rightarrow \pi^- \eta^{(\prime)} \nu_\tau$ Decays

This chapter provides a thorough examination of the $\tau^- \rightarrow \pi^- \eta^{(\prime)} \nu_\tau$ decays. We will start by writing the decay amplitude using effective Lagrangian, followed by a detailed discussion on the form factors involved in the said decays. We will use these amplitude and form factors to calculate different physical observables such as the Dalitz Plot, differential decay width, and forward-backward asymmetry. First, we introduce Dalitz plots to represent the phase space distribution of final state particles, offering insights into resonance structures and kinematic boundaries. Next, we discuss the differential decay width, crucial for predicting decay rates and understanding the kinematics of τ lepton decays. Additionally, we will discuss the forward-backward asymmetry associated with these decays. This asymmetry provides valuable information about the angular distribution of the decay products relative to the initial τ lepton direction, revealing underlying symmetries and dynamics. Throughout this chapter, our focus will be on establishing the theoretical framework and formalism necessary for a comprehensive understanding of $\tau^- \rightarrow \pi^- \eta^{(\prime)} \nu_\tau$ decays. Detailed discussions and interpretations of results will be presented in Chapter 5.

4.1 Amplitude of $\tau^- \rightarrow \pi^- \eta^{(\prime)} \nu_\tau$ Decays

For the semileptonic decay process $\tau^-(p) \rightarrow \pi^-(p_\pi) \eta^{(\prime)}(p_{\eta^{(\prime)}}) \nu_\tau(p_\nu)$, the decay amplitude is dominated by the vector, scalar, and tensor currents because of the parity properties of pseudoscalar mesons. The amplitude expression is given by:

$$\mathcal{M} = \mathcal{M}_V + \mathcal{M}_S + \mathcal{M}_T = \frac{G_F V_{ud} \sqrt{S_{EW}} (1 + \epsilon_L + \epsilon_R)}{\sqrt{2}} \times (L_\mu H^\mu + \hat{\epsilon}_S L H + 2\hat{\epsilon}_T L_{\mu\nu} H^{\mu\nu}) \quad (4.1)$$

In eq: (4.1) \mathcal{M}_V , \mathcal{M}_S , and \mathcal{M}_T represent the contributions from the vector, scalar, and tensor amplitude, respectively. Here, $S_{EW} = 1.0201(3)$ represents the electroweak correction factor [35], ϵ_L and ϵ_R refer to the left- and right-handed coupling constants, respectively, and $\hat{\epsilon}_S$ and $\hat{\epsilon}_T$ account for the scalar and tensor contributions.

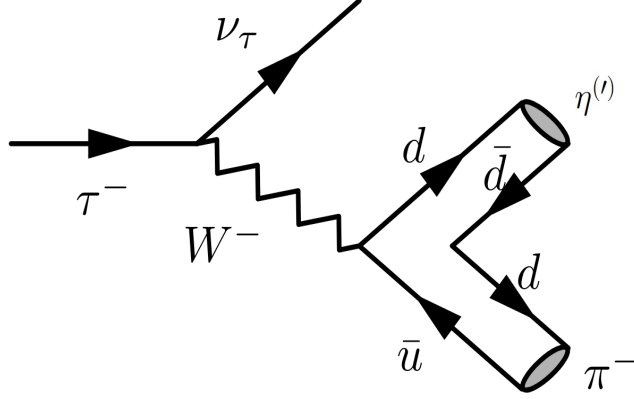


Figure 4.1: Feynman Diagram at Tree-Level for $\tau^- \rightarrow \pi^- \eta' \nu_\tau$ Decays

In the provided expression (4.1), the leptonic currents are expressed as follows:

$$L_\mu = \bar{u}(p_\nu) \gamma_\mu (1 - \gamma_5) u(p) \quad (4.2)$$

$$L = \bar{u}(p_\nu) (1 + \gamma_5) u(p) \quad (4.3)$$

$$L_{\mu\nu} = \bar{u}(p_\nu) \sigma_{\mu\nu} (1 + \gamma_5) u(p) \quad (4.4)$$

The tree-level Feynman diagram for $\tau^- \rightarrow \pi^- \eta' \nu_\tau$ decays is presented in Fig. (4.1). Additionally, the vector, scalar, and tensor hadronic matrix elements introduced in the equation 4.1 are defined as:

$$H^\mu = \langle \eta(\eta') \pi^- | \bar{d} \gamma^\mu u | 0 \rangle = c_V Q^\mu F_+(s) + c_S \frac{\Delta_{K^0 K^+}^{\text{QCD}}}{s} q^\mu F_0(s) \quad (4.5)$$

$$H = \langle \eta(\eta') \pi^- | \bar{d} u | 0 \rangle = F_S(s) \quad (4.6)$$

$$H^{\mu\nu} = \langle \eta(\eta') \pi^- | \bar{d} \sigma^{\mu\nu} u | 0 \rangle = i F_T(s) (p_\eta^\mu p_\pi^\nu - p_\pi^\mu p_\eta^\nu) \quad (4.7)$$

In our definitions, we introduce the following quantities: $s = q^2$, $q^\mu = (p_{\eta^{(\prime)}} + p_\pi)^\mu$, $Q^\mu = (p_{\eta^{(\prime)}} - p_\pi)^\mu + \frac{\Delta_{\pi^- \eta^{(\prime)}}}{s} q^\mu$, and $\Delta_{ij} \equiv m_i^2 - m_j^2$. Additionally, $\Delta_{K^0 K^+}^{\text{QCD}} = m_{K^0}^2 - m_{K^+}^2 + m_{\pi^+}^2 - m_{\pi^0}^2$. The constants $c_S = \sqrt{\frac{2}{3}}$ and $c_V = \sqrt{2}$ represent Clebsch-Gordan flavor coefficients. In η' case, $c_S = \frac{2}{\sqrt{3}}$ (while c_V remains $\sqrt{2}$).

The vector hadronic matrix element is ultimately expressed as:

$$\begin{aligned} \langle \pi^- \eta^{(\prime)} | \bar{d} \gamma^\mu u | 0 \rangle &= c_V^{\pi^- \eta^{(\prime)}} \left[(p_{\eta^{(\prime)}} - p_\pi)^\mu + \Delta_{\pi^- \eta^{(\prime)}} \frac{q^\mu}{s} \right] F_+^{\pi^- \eta^{(\prime)}}(s) \\ &+ c_S^{\pi^- \eta^{(\prime)}} \Delta_{K^0 K^+}^{\text{QCD}} \frac{q^\mu}{s} F_0^{\pi^- \eta^{(\prime)}}(s) \end{aligned} \quad (4.8)$$

In Eq. (4.8), the parameterization provides a significant advantage that the scalar (vector) form factor $F_{0(+)}^{\pi^- \eta^{(\prime)}}(s)$ corresponds to the final S (P)-wave state ($J = 0$ and $J = 1$), allowing for a clear distinction and characterization of the angular momentum properties and dynamics of the interaction or decay process under consideration. Furthermore, the requirement for matrix elements to remain finite at origin is:

$$F_+^{\pi^- \eta^{(\prime)}}(0) = -\frac{c_S^{\pi^- \eta^{(\prime)}}}{c_V^{\pi^- \eta^{(\prime)}}} \frac{\Delta_{K^0 K^+}^{\text{QCD}}}{\Delta_{\pi^- \eta^{(\prime)}}} F_0^{\pi^- \eta^{(\prime)}}(0) \quad (4.9)$$

The connection between the $F_0(s)$ and $F_S(s)$ form factors is established by the vector current's divergence through the relation:

$$F_S(s) = c_S \frac{\Delta_{K^0 K^+}^{\text{QCD}}}{(m_d - m_u)} F_0(s) \quad (4.10)$$

Utilizing known results from [36],

$$\begin{aligned} m_{\pi^+}^2 &= 2\hat{m}B, \\ m_{\pi^0}^2 &= 2\hat{m}B - \varepsilon + O(\varepsilon^2), \\ m_{K^+}^2 &= (m_u + m_s)B, \\ m_{K^0}^2 &= (m_d + m_s)B. \end{aligned} \quad (4.11)$$

it is evident that

$$\frac{\Delta_{K^0 K^+}^{\text{QCD}}}{(m_d - m_u)} = B \left(1 - \frac{1}{4} \frac{m_u - m_d}{m_s - \hat{m}} \right) \quad (4.12)$$

behaves approximately as B (3.9), where in eq. (4.11) $\hat{m} \equiv \frac{m_u + m_d}{2}$ and $\varepsilon = \frac{B}{4} \frac{(m_u - m_d)^2}{(m_s - \hat{m})}$. $BF^2 = \langle 0 | \bar{q}q | 0 \rangle$ is of the order of $-(270 \text{ MeV})^3$ [37]. Given that F is roughly 92 MeV, it follows that B is of the same order as M_τ . Consequently, $F_S(s)$ inherits the strong isospin suppression observed in $F_0(s)$. The scalar term in Eq. (4.6) may be effectively “absorbed” to the vector current amplitude by utilizing the Dirac equation $L = \frac{L_\mu q^\mu}{M_\tau}$ and Eq. (4.10). This can be accomplished by substituting

$$c_S \frac{\Delta_{K^0 K^+}^{\text{QCD}}}{s} \longrightarrow c_S \frac{\Delta_{K^0 K^+}^{\text{QCD}}}{s} \left(1 + \frac{s \hat{c}_S}{m_\tau (m_d - m_u)} \right) \quad (4.13)$$

into the second term of Eq. (4.5).

4.2 $\pi^-\eta^{(\prime)}$ Scalar Form Factor Using Breit-Wigner approach

We used the Resonance Chiral Theory (RChT) framework to describe the necessary scalar form factor (SFF) for $\pi^-\eta^{(\prime)}$. The SFFs are derived from [38]:

$$F_0^{\pi^-\eta^{(\prime)}}(s) = c_0^{\pi^-\eta^{(\prime)}} \left[1 + \frac{8c_m(c_d - c_m)}{F^2} \frac{2m_K^2 - m_\pi^2}{M_S^2} - \frac{4c_m(c_d - c_m)2m_\pi^2 + c_d(s + m_\pi^2 - m_{\eta^{(\prime)}}^2)}{F^2} \frac{1}{M_S^2 - s} \right] \quad (4.14)$$

In the $\pi\eta'$ channel, $c_0^{\pi^-\eta^{(\prime)}}$ is expressed as $\frac{\cos\theta_{\eta\eta'} + \sin\theta_{\eta\eta'}}{\sqrt{2}}$, while for the $\pi\eta$ channel, $c_0^{\pi^-\eta}$ takes the form $\cos\theta_{\eta\eta'} - \sqrt{2}\sin\theta_{\eta\eta'}$. Additionally, $c_d(m)$ denotes the couplings present in the Lagrangian's derivative (mass) terms, which involve the nonets of pseudoscalar and scalar mesons. Upon imposing the QCD asymptotic behavior of the form factors, characterized by $O(1/s)$ for large s , resulting in $c_d - c_m = 0$ and $4c_dc_m = F^2$, we deduce $c_d = c_m = F/2$ [39], they are eventually stated as:

$$F_0^{\pi^-\eta^{(\prime)}}(s) = c_0^{\pi^-\eta^{(\prime)}} \left(1 + \frac{\Delta_{\pi^-\eta^{(\prime)}}}{M_S^2} \right) \frac{M_S^2}{M_S^2 - s} \quad (4.15)$$

and at the origin their values are

$$F_0^{\pi^-\eta^{(\prime)}}(0) = c_0^{\pi^-\eta^{(\prime)}} \left(1 + \frac{\Delta_{\pi^-\eta^{(\prime)}}}{M_S^2} \right) \quad (4.16)$$

Incorporating these normalizations into Eq. (4.9) yields an estimation of the normalizations of associated vector form factors:

$$\begin{aligned} F_+^{\pi^-\eta}(0) &= -\cos\theta_{\eta\eta'} - \frac{\sqrt{2}\sin\theta_{\eta\eta'}}{\sqrt{3}} \Delta_{K^0K^+}^{\text{QCD}} \Delta_{\pi^-\eta} \left(1 + \frac{\Delta_{\pi^-\eta}}{M_S^2} \right) \\ &= \cos\phi_{\eta\eta'} \frac{m_{K^0}^2 - m_{K^+}^2 - m_{\pi^0}^2 + m_{\pi^+}^2}{m_\eta^2 - m_{\pi^-}^2} \left(1 - \frac{m_\eta^2 - m_{\pi^-}^2}{M_S^2} \right) \end{aligned} \quad (4.17)$$

and

$$\begin{aligned} F_+^{\pi^-\eta'}(0) &= -\sin\theta_{\eta\eta'} + \frac{\sqrt{2}\cos\theta_{\eta\eta'}}{\sqrt{3}} \Delta_{K^0K^+}^{\text{QCD}} \Delta_{\pi^-\eta'} \left(1 + \frac{\Delta_{\pi^-\eta'}}{M_S^2} \right) \\ &= \sin\phi_{\eta\eta'} \frac{m_{K^0}^2 - m_{K^+}^2 - m_{\pi^0}^2 + m_{\pi^+}^2}{m_\eta^2 - m_{\pi^-}^2} \left(1 - \frac{m_{\eta'}^2 - m_{\pi^-}^2}{M_S^2} \right) \end{aligned} \quad (4.18)$$

For simplicity, η - η' mixing in the quark-flavor basis is, $\cos \phi_{\eta\eta'} = \frac{\cos \theta_{\eta\eta'} - \sqrt{2} \sin \theta_{\eta\eta'}}{\sqrt{3}}$ and $\sin \phi_{\eta\eta'} = \frac{\sin \theta_{\eta\eta'} + \sqrt{2} \cos \theta_{\eta\eta'}}{\sqrt{3}}$. When comparing these VFF normalizations to those derived following Eq. (4.26), one gets:

$$\epsilon_{\pi\eta^{(\prime)}} = \cos \phi_{\eta\eta'} (\sin \phi_{\eta\eta'}) \frac{m_{K^0}^2 - m_{K^+}^2 - m_{\pi^0}^2 + m_{\pi^+}^2}{m_{\eta^{(\prime)}}^2 - m_{\pi^-}^2} \left(1 - \frac{m_{\eta^{(\prime)}}^2 - m_{\pi^-}^2}{M_S^2} \right) \quad (4.19)$$

From Eq. (4.19), we can derive numerical estimates for the $\pi\eta(\eta')$ mixing angles. Specifically, we find $\epsilon_{\pi\eta} = (9.8 \pm 0.3) \times 10^{-3}$ and $\epsilon_{\pi\eta'} = (2.5 \pm 1.5) \times 10^{-4}$. Notably, these values, particularly in the case of $\epsilon_{\pi\eta'}$, deviate significantly from their values in the infinite scalar mass limit, denoted as $\hat{\epsilon}_{\pi\eta}$ and $\hat{\epsilon}_{\pi\eta'}$, respectively, which are 0.014 and 0.0038, as reported in Ref.[40]. These calculations were based on $\phi_{\eta\eta'} = (41.4 \pm 0.5)^\circ$ [41]. Notably, $\epsilon_{\pi\eta'}$ is observed to be one order of magnitude less than $\hat{\epsilon}_{\pi\eta'}$, primarily due to the significant suppression arising from $m_{\eta'} \approx M_S$. The SFFs as shown in Eq. (4.15) start to lose accuracy near the resonance region. It becomes inadequate when $s = M_S^2$, where M_S represents an on-shell intermediate scalar resonance. A standard and straightforward approach to address this constraint is by upgrading the scalar propagator $\frac{1}{M_S^2 - s}$ to $\frac{1}{M_S^2 - s - iM_S\Gamma_S(s)}$, here the associated energy-dependent width, calculated using RChT, is given by:

$$\Gamma_S(s) = \Gamma_S(M_S^2) \left(\frac{s}{M_S^2} \right)^{3/2} \frac{h(s)}{h(M_S^2)} \quad (4.20)$$

The function $h(s)$ is defined as:

$$\begin{aligned} h(s) = & \sigma_{K^-K^0}(s) + 2 \cos^2 \phi_{\eta\eta'} \left(1 + \frac{\Delta_{\pi^- \eta}}{s} \right)^2 \sigma_{\pi^- \eta}(s) \\ & + 2 \sin^2 \phi_{\eta\eta'} \left(1 + \frac{\Delta_{\pi^- \eta'}}{s} \right)^2 \sigma_{\pi^- \eta'}(s) \end{aligned} \quad (4.21)$$

where the kinematical factor $\sigma_{PQ}(s)$ is given by:

$$\sigma_{PQ}(s) = \frac{2q_{PQ}(s)}{\sqrt{s}} \Theta(s - (m_P + m_Q)^2) \quad (4.22)$$

The $a_0(980)$ resonance is characterized by a Breit-Wigner mass of $M_S = (980 \pm 20)$ MeV and a width of $\Gamma_S = (75 \pm 25)$ MeV [20], we estimate the scalar form factors at origin, as per Eq. (4.16), to be $F_0^{\pi\eta}(0) = 0.92 \pm 0.02$ and $F_0^{\pi\eta'}(0) = 0.05 \pm 0.03$, respectively. the resultant scalar form factors are indistinguishable within the context of RChT. meaning $\tilde{F}_0^{\pi^- \eta}(s) = \tilde{F}_0^{\pi^- \eta'}(s)$. Figure 4.2 shows a graphic representation of the mediated scalar resonance $a_0(980)$.

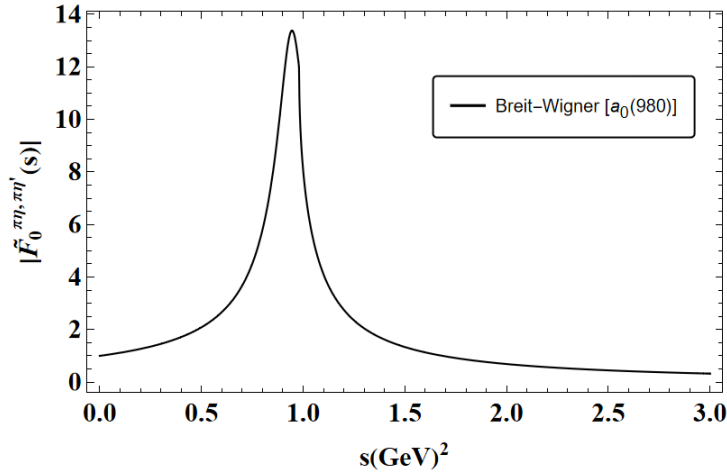


Figure 4.2: The normalized scalar form factor for $\pi^-\eta'$, derived using the Breit-Wigner approach outlined in Section 4.2

Additional resonances having similar quantum numbers as the $a_0(980)$ can be included in this description. In particular, we include the $a_0(1450)$ resonance, whose effects might be observed in the phase space that is accessible, even if it is massive. Resonances beyond this point will not be taken into consideration for the same reason, though. Within the context of RChT, the SFFs containing two resonances are written as follows:

$$\begin{aligned}
F_0^{\pi^-\eta^{(\prime)}}(s) &= c_0^{\pi^-\eta^{(\prime)}} \\
&\times \left[1 + \frac{8c_m(c_d - c_m)}{F^2} \frac{2m_K^2 - m_\pi^2}{M_S^2} - \frac{4c_m(c_d - c_m)2m_\pi^2 + c_d(s + m_\pi^2 - m_{\eta^{(\prime)}}^2)}{F^2 M_S - s} \right. \\
&\left. + \frac{8c'_m(c'_d - c'_m)}{F^2} \frac{2m_K^2 - m_\pi^2}{M_{S'}^2} - \frac{4c'_m(c'_d - c'_m)2m_\pi^2 + c'_d(s + m_\pi^2 - m_{\eta^{(\prime)}}^2)}{F^2 M_{S'} - s} \right] \quad (4.23)
\end{aligned}$$

here S and S' stand for the resonances associated with $a_0(980)$ and $a_0(1450)$, respectively. The limits imposed by the short-distance condition for form factors approaching 0 as $s \rightarrow \infty$ are:

$$4c_d c_m + 4c'_m c'_d = F^2, \quad c_m \frac{M_S^2}{(c_m - c_d)} + c'_m \frac{M_{S'}^2}{(c'_m - c'_d)} = 0. \quad (4.24)$$

The couplings c'_d and c'_m , with c_d and c_m to a lesser extent, are not well understood in terms of their precise values. It is possible to keep this constraint for two

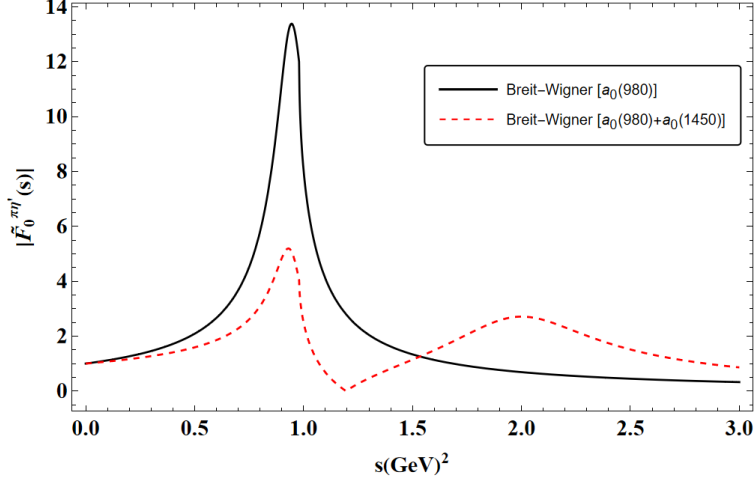


Figure 4.3: The Breit-Wigner method, detailed in Section 4.2, yielded normalized $\pi^-\eta'$ scalar form factors with two resonances (red dashed curve) and one resonance (solid black curve), respectively.

resonances if we assume the single-resonance case's requirement $c_d = c_m$. As a result, $c'_d = c'_m$. As a result, the SFFs are represented by:

$$\begin{aligned}
F_0^{\pi^-\eta^{(\prime)}}(s) &= c_0^{\pi^-\eta^{(\prime)}} \left[1 + \frac{4}{F^2} \left(\frac{c_m^2}{M_S^2 - s} + \frac{c'_m{}^2}{M_{S'}^2 - s} \right) (s + m_\pi^2 - m_{\eta^{(\prime)}}^2) \right] \\
&\rightarrow \frac{c_0^{\pi^-\eta^{(\prime)}}}{(M_S^2 - s - iM_S\Gamma_S(s))(M_{S'}^2 - s - iM_{S'}\Gamma_{S'}(s))} \{ (M_S^2 - s)(M_{S'}^2 - s) \\
&\quad + \frac{4}{F^2} [c_m^2(M_{S'}^2 - s) + c'_m{}^2(M_S^2 - s)](s + m_\pi^2 - m_{\eta^{(\prime)}}^2) \}
\end{aligned} \tag{4.25}$$

Here, we incorporated energy-dependent widths into the scalar propagators. Numerically, the scalar coupling is set to $c_m = 41.9$ MeV and for the $a_0(1450)$ resonance, the mass $M_{S'} = (1474 \pm 19)$ MeV and the width $\Gamma_{S'} = (265 \pm 13)$ MeV are used. Figure 4.3 shows the normalized SFFs for $\pi\eta^{(\prime)}$ computed from Equation (4.25), taking two resonances, and compares it to the single-resonance scenario. A notable feature of the normalized expressions is their mode-dependent behavior: in the $\pi\eta'$ case, in fig. 4.3, two comparable peaks surrounding both resonances are observed, whereas, in $\pi\eta$ scenario, there is a dominant peak for resonance $a_0(980)$ and a smaller peak associated with the $a_0(1450)$ are seen in fig. 4.4.

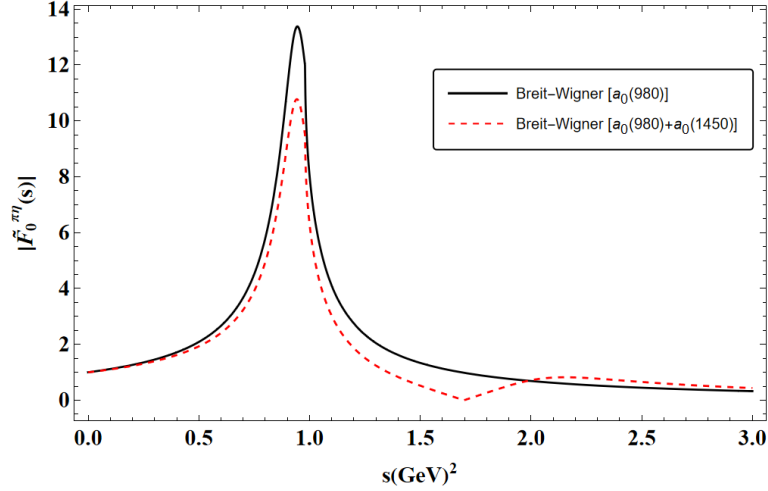


Figure 4.4: The Breit-Wigner method, detailed in Section 4.2, yielded normalized $\pi^-\eta$ scalar form factors with two resonances (red dashed curve) and one resonance (solid black curve), respectively.

4.3 Vector Form Factor for $\pi^-\eta^{(\prime)}$

We will employ the VFF for $\pi^-\eta^{(\prime)}$ within the context of RChT that incorporates resonances as explicit degrees of freedom [38], which is expressed as:

$$F_+^{\pi^-\eta^{(\prime)}}(s) = \varepsilon_{\pi\eta^{(\prime)}} \left(1 + \sum_V \frac{F_V G_V}{F^2} \frac{s}{M_V^2 - s} \right) \quad (4.26)$$

where $\varepsilon_{\pi\eta^{(\prime)}}$ represents the contribution through π^0 - η - η' mixing, the brackets include the interchange of an infinite series of vector resonances arranged in nonets, as well as the direct contact term. Here F_V and G_V denote the two coupling constants of the Lagrangian that couples one nonet of vectors to pseudoscalars, and M_V is the mass of the nonet vector).

At this stage, several alternatives for incorporating the resonance width appear. The simplest solution is to substitute $M_V^2 - s$ with $M_V^2 - s - iM_V\Gamma_S(s)$ in equation (4.26). We will refer to this alternative as the “dipole model” or the “Breit-Wigner (BW) model”.

$$F_+^{\pi^-\eta^{(\prime)}}(s) = \varepsilon_{\pi\eta^{(\prime)}} \left(1 + \sum_V \frac{F_V G_V}{F^2} \frac{s}{M_V^2 - s - iM_V\Gamma_S(s)} \right) \quad (4.27)$$

By incorporating the vector resonant contribution provided by $\rho(770)$ of which the influence is apparent from the clear peak of about 0.5 GeV^2 , and its higher radial excitation $\rho'(1450)$ is seen around 1.9 GeV^2 in fig. (4.5).

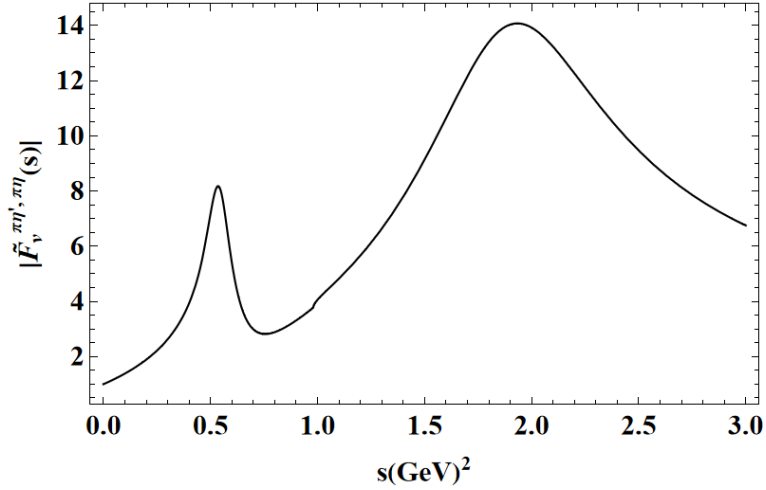


Figure 4.5: $\pi^-\eta^{(\prime)}$ VFF as obtained by using Breit-Wigner approach

Notably, the term in the parentheses in Eq. (4.26) resembles the computation of $\pi^-\pi^0$ VFF. Consequently, the vector form factors for $\pi^-\eta^{(\prime)}$ can be expressed using the well-known $\pi^-\pi^0$ VFF. This results in their equality at zero momentum transfer, $F_+^{\pi^-\eta^{(\prime)}}(0) = \varepsilon_{\pi\eta^{(\prime)}}$ and leads to normalized form factors:

$$\tilde{F}_+^{\pi^-\eta'}(s) = \tilde{F}_+^{\pi^-\eta}(s) = \tilde{F}_+^{\pi^-\pi^0}(s) \quad (4.28)$$

This relation allows us to explain the $\pi^-\eta'$ decay modes of interest using well-established experimental data on VFF for $\pi^-\pi^0$. Specifically, we utilize the most recent experimental data from the Belle Collaboration's analysis of the decay process $\tau^- \rightarrow \pi^-\pi^0\nu_\tau$, which helps to explain the impacts of larger radial excitations and the predominate vector resonant contributions [42].

4.4 Tensor Form Factor (TFF) for $\pi^-\eta^{(\prime)}$

Remarkably, the effects of non-standard (NS) scalar interactions are found to develop linearly to the variable s . Conversely, when considering final states involving $\pi^-\eta^{(\prime)}$, the presence of isospin asymmetry leads to a suppression of the SFF $F_0(s)$, while the contribution of new scalar interactions appears at $O(0)$ with respect to the isospin breaking parameter. Hence, the isospin-breaking $\tau^- \rightarrow \pi^-\eta^{(\prime)}\nu_\tau$ decays are expected to exhibit sensitivity to scalar interactions. The TFF, which describes the hadronization of the tensor current, is derived using the leading chiral Lagrangian; $\mathcal{L}^{O(p^4)} = \Lambda_1 \langle t_+^{\mu\nu} f_{+\mu\nu} \rangle - i\Lambda_2 \langle t_+^{\mu\nu} u_\mu u_\nu \rangle$: $F_T^{\eta\pi^-}(0) = \epsilon_{\pi\eta} F_T^{\pi^0\pi^-}(0) = \frac{\sqrt{2}\Lambda_2}{F^2}$ [26].

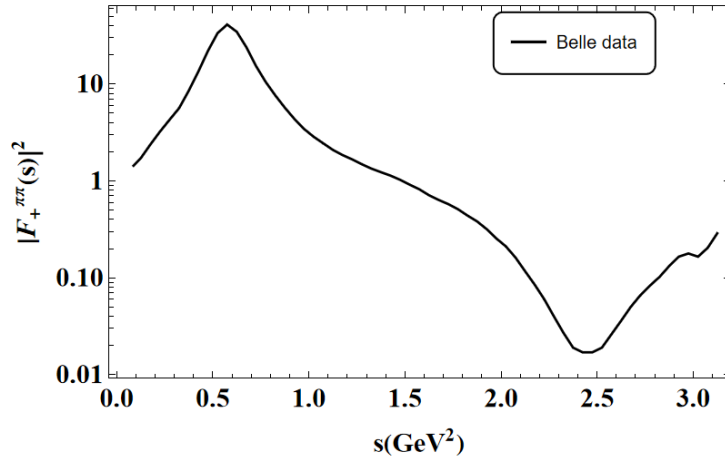


Figure 4.6: The vector form factor $\pi^-\pi^0$ found by the Belle Collaboration

The tensor form factor has minimal impact on $\tau^- \rightarrow \pi^-\eta(\eta')\nu_\tau$ decays, making precise normalization and s -dependence less important. So, we will ignore the s -dependence, namely $F_T^{\pi\eta^{(\prime)}}(s) = F_T^{\pi\eta^{(\prime)}}(0) \equiv F_T^{\pi\eta^{(\prime)}}$. This leads to $|F_T^{\pi\eta}| \leq 0.094 \text{ GeV}^{-1}$ and $|F_T^{\pi\eta'}| \leq 2.4 \times 10^{-3} \text{ GeV}^{-1}$. However, if tilded form factors are used instead, $|\tilde{F}_T^{\pi\eta}| = |\tilde{F}_T^{\pi\eta'}| = \sqrt{2}\Lambda_2/F^2 = 9.59 \text{ GeV}^{-1}$.

4.5 Physical Observables

To explore NP effects in $\tau^- \rightarrow \pi^-\eta^{(\prime)}\nu_\tau$ decays, we must analyze not only the hadronic spectrum and branching ratio but also Dalitz plot distributions and the forward-backward asymmetry. This section examines the impact of NS scalar and tensor couplings from Chapter 3 on these physical observables. We begin with the Dalitz plots and then proceed to integrated observables, focusing on the differential decay width as a function of the hadronic invariant mass and the forward-backward asymmetry. The differential decay rate for $\tau^- \rightarrow \pi^-\eta^{(\prime)}\nu_\tau$ decays within the rest frame of τ lepton is as follows:

$$\frac{d^2\Gamma}{dsdt} = \frac{1}{32(2\pi)^3 M_\tau^3} |\mathcal{M}|^2 \quad (4.29)$$

here, $|\mathcal{M}|^2$ signifies the squared matrix element averaged over spin states, without considering polarization effects. The variable s represents the invariant mass of the hadronic system, ranging as $(m_{\eta^{(\prime)}} + m_\pi)^2 \leq s \leq M_\tau^2$. Additionally, $t = (p' + p_{\eta^{(\prime)}})^2 = (p - p_{\pi^-})^2$, where t is the Mandelstam variable representing the

momentum transfer squared. The kinematic boundaries are defined as $t_-(s) \leq t \leq t_+(s)$. Their expressions are as follows:

$$t_{\pm}(s) = \frac{1}{2s} \left[2s(M_{\tau}^2 + m_{\pi}^2) - (M_{\tau}^2 + s)(s + m_{\pi}^2 - m_{\eta^{(\prime)}}^2) \pm (M_{\tau}^2 - s) \sqrt{\lambda(s, m_{\pi}^2, m_{\eta^{(\prime)}}^2)} \right], \quad (4.30)$$

where the Kallen function, denoted as $\lambda(\alpha, \beta, \gamma)$, is expressed as: $\lambda(\alpha, \beta, \gamma) = \alpha^2 + \beta^2 + \gamma^2 - 2\alpha\beta - 2\alpha\gamma - 2\beta\gamma$.

4.5.1 Dalitz plots

When examining τ decays including scalar, vector, and tensor currents (SCC), Dalitz plots are essential for some reasons:

Characterizing Hadronic Dynamics: The distribution of decay products in the phase space can be seen graphically with Dalitz plots. The kinematics of the decay process, including the relative contributions from various intermediate states and resonances, can be better understood by analyzing these plots.

Identifying Resonant Structures: In Dalitz plots, resonant structures can reveal the existence of certain particles or resonances that are essential to the decay process. By examining these structures, one may be able to find novel resonances as well as identify and characterize the particles causing the decay.

Testing Standard Model Predictions: The distributions and rates of τ decays are predicted by the Standard Model (SM). Variations from these predictions in Dalitz plots may indicate the presence of NP. By examining experimental Dalitz plots in comparison to theoretical predictions, one can assess the SM's validity and look for indications of new physics.

Searching for New Physics: Dalitz plot anomalies could be signs of new physics phenomena, including interactions mediated by hypothetical particles not included in the Standard Model. By examining these graphs, one can look for indications of new physics, such as consequences from theories like extra dimensions, supersymmetry, or dark matter particle interactions.

Measuring Decay Parameters: Dalitz plots offer a way to extract critical decay parameters, including angular distributions, decay rates, and branching fractions. Accurate measurements of these factors increase our understanding of fundamental basic interactions.

The unpolarized squared amplitude averaged over spins in the presence of New Physics interactions is given by:

$$|\mathcal{M}|^2 = \frac{2G_F^2 |V_{ud}|^2 S_{EW} (1 + \epsilon_L + \epsilon_R)^2}{s^2} \times (M_{0+} + M_{T+} + M_{T0} + M_{00} + M_{++} + M_{TT}) \quad (4.31)$$

Here, M_{++} , M_{00} , and M_{TT} are the vector, scalar, and tensor contributions to the amplitude, respectively, while their corresponding interference terms are denoted by M_{0+} , M_{T+} , M_{T0} . Their detailed expressions are:

$$\begin{aligned}
M_{0+} &= 2c_V c_S m_\tau^2 \text{Re}[F_+(s)F_0^*(s)] \Delta_{K^0 K^+}^{QCD} \left(1 + s \frac{\hat{\epsilon}_S}{m_\tau(m_d - m_u)} \right) \\
&\quad \times (s(m_\tau^2 - s + \Sigma_{\pi\eta^{(\nu)}}) - 2t) + m_\tau^2 \Delta_{\pi\eta^{(\nu)}}), \\
M_{T+} &= -4c_V \hat{\epsilon}_T m_\tau^3 s \text{Re}[F_T F_+^*(s)] \left(1 - \frac{s}{m_\tau^2} \right) \lambda(s, m_\pi^2, m_{\eta^{(\nu)}}^2), \\
M_{T0} &= -4c_S \Delta_{K^0 K^+}^{QCD} \hat{\epsilon}_T m_\tau s \text{Re}[F_T F_0^*(s)] \left(1 + \frac{s \hat{\epsilon}_S}{m_\tau(m_d - m_u)} \right) \\
&\quad \times (s(m_\tau^2 - s - 2t + \Sigma_{\pi\eta^{(\nu)}}) + m_\tau^2 \Delta_{\pi\eta^{(\nu)}}), \\
M_{00} &= c_S^2 (\Delta_{K^0 K^+}^{QCD})^2 m_\tau^4 \left(1 - \frac{s}{m_\tau^2} \right) |F_0(s)|^2 \left(1 + \hat{\epsilon}_S \frac{s}{m_\tau(m_d - m_u)} \right)^2, \\
M_{++} &= c_V^2 |F_+(s)|^2 \left[m_\tau^4 (s + \Delta_{\pi\eta^{(\nu)}})^2 - m_\tau^2 s (2\Delta_{\pi\eta^{(\nu)}}(s + 2t - 2m_\pi^2) \right. \\
&\quad \left. + \Delta_{\pi\eta^{(\nu)}}^2 + s(s + 4t)) \right] + 4m_{\eta^{(\nu)}}^2 s^2 (m_\pi^2 - t) + 4s^2 t (s + t - m_\pi^2), \\
M_{TT} &= -\hat{\epsilon}_T^2 F_T^2 s^2 (m_\pi^2 - s)^2 (-m_\tau^2 + s) + m_{\eta^{(\nu)}}^4 (3m_\tau^2 + s) \\
&\quad + 4(m_\pi^2 - s)(m_\tau^2 - s)t + 4st^2 + 2m_{\eta^{(\nu)}}^2 (-((m_\pi^2 - 2m_\tau^2 - s)(m_\tau^2 - s)) \\
&\quad - 2(m_\tau^2 + s)t)
\end{aligned} \tag{4.32}$$

The defined quantities $\Delta_{\pi\eta^{(\nu)}} = m_{\pi^-}^2 - m_{\eta^{(\nu)}}^2$ and $\Sigma_{\pi\eta^{(\nu)}} = m_{\pi^-}^2 + m_{\eta^{(\nu)}}^2$. NP effects might be visible in the distribution of Dalitz plots, particularly through a significant enhancement towards higher values of the hadronic invariant mass, as suggested by eq. (4.13).

4.5.2 Angular Distribution

New Physics contributions also modify the hadronic mass and angular distributions of decay products, potentially providing different sensitivities to scalar and tensor interactions. To simplify the analysis, it is advantageous to work in the hadronic system's rest frame, which is defined as $\vec{p}_\pi + \vec{p}_{\eta^{(\nu)}} = \vec{p}_{\tau^-} - \vec{p}_{\nu_\tau} = 0$. Within this framework, the energies of the τ lepton and pion are expressed as follows:

$$E_\tau = \frac{s + M_\tau^2}{2\sqrt{s}}, \quad E_\pi = \frac{s + m_\pi^2 - m_{\eta^{(\nu)}}^2}{2\sqrt{s}} \tag{4.33}$$

The angle θ between the τ lepton and three-momenta of the pion is related to the invariant variable t through:

$$t = m_\tau^2 + m_\pi^2 - 2E_\tau E_\pi + 2|\vec{p}_\pi||\vec{p}_\tau| \cos \theta \quad (4.34)$$

here, $|\vec{p}_\pi| = \sqrt{E_\pi^2 - m_\pi^2}$ and $|\vec{p}_\tau| = \sqrt{E_\tau^2 - m_\tau^2}$. The decay distribution for the variables $(s, \cos \theta)$, considering the most generic effective interactions is expressed as:

$$\begin{aligned} \frac{d^2\Gamma}{dsd\cos\theta} &= \frac{G_F^2 |V_{ud}|^2 S_{EW}}{128\pi^3 m_\tau} (1 + \epsilon_L + \epsilon_R)^2 \left(\frac{m_\tau^2}{s} - 1\right)^2 |\vec{p}_\pi| \left\{ (c_S \Delta_{K^0 K^+}^{QCD})^2 |F_0^{\pi^- \eta^{(\prime)}}(s)|^2 \right. \\ &\times \left(1 + \frac{s \hat{\epsilon}_S}{m_\tau(m_d - m_u)}\right)^2 + 16|\vec{p}_\pi|^2 s^2 \left| \frac{c_V}{2m_\tau} F_+^{\pi^- \eta^{(\prime)}}(s) - \hat{\epsilon}_T F_T \right|^2 \\ &+ 4|\vec{p}_\pi|^2 s \left(1 - \frac{s}{m_\tau^2}\right) \left[c_V^2 |F_+^{\pi^- \eta^{(\prime)}}(s)|^2 + 4\hat{\epsilon}_T F_T^2 s \right] \cos^2 \theta \\ &+ 4c_S \Delta_{K^0 K^+}^{QCD} |\vec{p}_\pi| \sqrt{s} \cos \theta \times \left(1 + \frac{s}{m_\tau(m_d - m_u)} \hat{\epsilon}_S\right) \\ &\left. \left[c_V \text{Re}[F_+^*(s) F_0(s)] - 2\frac{s}{m_\tau} \hat{\epsilon}_T F_T \text{Re}[F_0(s)] \right] \right\} \end{aligned} \quad (4.35)$$

Setting the effective couplings to zero retrieves the usual expressions for this observable within the Standard Model. Significantly, the emergence of new interactions does not introduce any new angular dependencies. However, the coefficients associated with the $\cos \theta$ terms are adjusted due to terms that scale with the hadronic invariant mass s . In the absence of new physics, the last term of the preceding equation, linear in $\cos \theta$, has the potential to probe the relative phase between the vector and scalar contributions.

4.5.3 Decay Width

Integrating Eq. (4.29) across the variable t yields the hadronic invariant mass distribution:

$$\begin{aligned} \frac{d\Gamma}{ds} &= \frac{G_F^2 S_{EW} m_\tau^3 |V_{ud} F_+^{\pi^- \eta^{(\prime)}}(0)|^2}{384\pi^3 s} (1 + \epsilon_L + \epsilon_R)^2 \left(1 - \frac{s}{m_\tau^2}\right)^2 \\ &\times \lambda^{1/2}(s, m_{\eta^{(\prime)}}^2, m_\pi^2) [Y_{VA} + \hat{\epsilon}_S Y_S + \hat{\epsilon}_T Y_T + \hat{\epsilon}_S^2 Y_{S^2} + \hat{\epsilon}_T^2 Y_{T^2}] \end{aligned} \quad (4.36)$$

where

$$\begin{aligned}
Y_{VA} &= \frac{1}{s^2} \left[3 \left| \tilde{F}_0^{\pi^- \eta^{(\prime)}}(s) \right|^2 \Delta_{\pi^- \eta^{(\prime)}}^2 + \left| \tilde{F}_+^{\pi^- \eta^{(\prime)}}(s) \right|^2 \lambda(s, m_{\eta^{(\prime)}}^2, m_\pi^2) \left(1 + \frac{2s}{m_\tau^2} \right) \right] \\
Y_S &= \frac{6}{sm_\tau} \left| \tilde{F}_0^{\pi^- \eta^{(\prime)}}(s) \right|^2 \frac{\Delta_{\pi^- \eta^{(\prime)}}^2}{m_d - m_u} \\
Y_T &= \frac{-6\sqrt{2} \operatorname{Re} [F_+(s)] F_T}{sm_\tau \left| F_+^{\pi^- \eta^{(\prime)}}(0) \right|^2} \lambda(s, m_{\eta^{(\prime)}}^2, m_\pi^2) \\
Y_{S^2} &= \frac{3}{m_\tau^2} \left| \tilde{F}_0^{\pi^- \eta^{(\prime)}}(s) \right|^2 \frac{\Delta_{\pi^- \eta^{(\prime)}}^2}{(m_d - m_u)^2} \\
Y_{T^2} &= \frac{4}{s} \frac{|F_T|^2}{|F_+(0)|^2} \left(1 + \frac{s}{2m_\tau^2} \right) \lambda(s, m_{\eta^{(\prime)}}^2, m_\pi^2)
\end{aligned} \tag{4.37}$$

Notice that when $\epsilon_L = \epsilon_R = \hat{\epsilon}_S = \hat{\epsilon}_T = 0$, the Standard Model result is recovered. Furthermore, by considering the matrix element to be finite at origin and the normalization of form factors, we observe that [38]:

$$F_+^{\pi^- \eta^{(\prime)}}(0) = -\frac{c_{\pi^- \eta^{(\prime)}}^S}{c_{\pi^- \eta^{(\prime)}}^V} \frac{\Delta_{K^0 K^+}^{\text{QCD}}}{\Delta_{\pi^- \eta^{(\prime)}}} F_0^{\pi^- \eta^{(\prime)}}(0) \tag{4.38}$$

and

$$\tilde{F}_{\pi^- \eta^{(\prime)}}^{+,0}(s) = \frac{F_{\pi^- \eta^{(\prime)}}^{+,0}(s)}{F_{\pi^- \eta^{(\prime)}}^{+,0}(0)} \tag{4.39}$$

which are employed to express eq. (4.36). The scalar, vector, and tensor form factors, detailed in Sections 4.2, 4.3 and 4.4, finally entered in Eq.(4.36) for predicting the partial decay rate of $\tau^- \rightarrow \pi^- \eta^{(\prime)} \nu_\tau$ decays.

4.5.4 Forward-Backward Assymetry (A_{FB})

A_{FB} is a key finding in high-energy physics, as it provides insights into the underlying dynamics of particle interactions. It is the difference in the angular distribution of final-state particles produced by a collision between the forward and backward directions relative to the initial collision axis.

Consider a generic particle collision process $ab \rightarrow X$, where a and b are incoming particles and X represents the final-state particles. The forward direction is defined as the direction of motion of particle X relative to the incoming particle a , while the backward direction is defined similarly with respect to particle b .

The forward-backward asymmetry is quantified as:

$$A_{FB} = \frac{N_F - N_B}{N_F + N_B} \quad (4.40)$$

Here, N_F and N_B represent the number of final-state particles observed in the forward and backward directions, expressed as:

$$N_F = \int_0^1 \frac{d^2\Gamma}{dsd\cos\theta} d\cos\theta, \quad N_B = \int_{-1}^0 \frac{d^2\Gamma}{dsd\cos\theta} d\cos\theta \quad (4.41)$$

A_{FB} is critical for validating theoretical predictions and exploring NP. Deviations from the expected asymmetry values could imply the existence of additional particles or interactions not accounted for by existing theoretical models.

Experimental collaborations at particle colliders, including the LHC, have focused on precisely measuring forward-backward asymmetries in various collision processes. These measurements significantly contribute to understanding fundamental interactions and discovering new physics.

In summary, A_{FB} is a key observable in high-energy physics that provides valuable information about the underlying dynamics of particle interactions and serves as a sensitive probe for new physics phenomena. The A_{FB} is defined [43] as:

$$A_{FB} = \frac{\int_0^1 d\cos\theta \frac{d^2\Gamma}{dsd\cos\theta} - \int_{-1}^0 d\cos\theta \frac{d^2\Gamma}{dsd\cos\theta}}{\int_0^1 d\cos\theta \frac{d^2\Gamma}{dsd\cos\theta} + \int_{-1}^0 d\cos\theta \frac{d^2\Gamma}{dsd\cos\theta}} \quad (4.42)$$

For $\tau^- \rightarrow \pi^- \eta^{(\prime)} \nu_\tau$ decays, we can derive it by putting eq. (4.35) in eq. (4.42) and then it integrate over the $\cos\theta$

$$A_{FB}^{\pi\eta^{(\prime)}}(s) = \frac{-3c_S \sqrt{\lambda(s, m_{\pi^-}^2, m_{\eta^{(\prime)}}^2)}}{2s^2 [Y_{VA} + \hat{\epsilon}_S Y_S + \hat{\epsilon}_T Y_T + \hat{\epsilon}_S^2 Y_{S^2} + \hat{\epsilon}_T^2 Y_{T^2}]} \left(1 + \frac{s\hat{\epsilon}_S}{m_\tau(m_d - m_u)} \right) \\ \times \Delta_{\pi-\eta^{(\prime)}} \left\{ c_V \text{Re} [F_+^*(s)F_0(s)] + \frac{2s\hat{\epsilon}_T}{m_\tau} \text{Re} [F_0^*(s)F_T(s)] \right\} \quad (4.43)$$

Once again, the A_{FB} within the SM is evident when $\epsilon_R = \epsilon_L = \hat{\epsilon}_S = \hat{\epsilon}_T = 0$ (which was initially investigated in [44]).

Chapter 5

Phenomenological Analysis of $\tau^- \rightarrow \pi^- \eta^{(\prime)} \nu_\tau$ Decays

This chapter presents the analysis of physical observables previously discussed in Chapter 4. These include Dalitz plot distributions, differential decay width, and the forward-backward asymmetry analysis for $\tau^- \rightarrow \pi^- \eta^{(\prime)} \nu_\tau$ decays. Our focus will be on examining these observables in the framework of new physics coefficients.

5.1 Dalitz Plot Analysis

Figure 5.1 shows the Dalitz plot distributions of $|\mathcal{M}|^2$ for the decay $\tau^- \rightarrow \pi^- \eta' \nu_\tau$, as discussed in subsection (4.5.1). The plots depict the squared matrix element $|\mathcal{M}|^2$ as a function of s and t Mandelstam variables, each representing different scenarios with varying scalar and tensor coefficients:

1. Figure 5.1(a) represents the SM scenario without new physics contributions $\hat{e}_S = \hat{e}_T = 0$.
2. Figure 5.1(b) shows $|\mathcal{M}|^2$ distribution with a scalar coefficient $\hat{e}_S = 0.006$, while $\hat{e}_T = 0$, introducing a scalar interaction.
3. Figure 5.1(c) depicts $|\mathcal{M}|^2$ distribution with a tensor coefficient $\hat{e}_T = 0.3$, and $\hat{e}_S = 0$, introducing a tensor interaction.

On the x-axis, s is the invariant mass of the $\pi^- \eta'$ system and on the y-axis, t represents the squared momentum transfer, both the variables are normalized to m_τ^2 . The color legend represents the magnitude of $|\mathcal{M}|^2$, ranging from lower values in blue to higher values in red. In 5.1(a), higher values are concentrated in the central region of the plot, indicating where the decay is most likely to occur. In

5.1(b), the scalar interaction seems to shift slightly and spread the high-value regions compared to the SM case, but overall the pattern is similar to the SM case. In 5.1(c), the tensor interaction appears to have a similar effect to the scalar interaction.

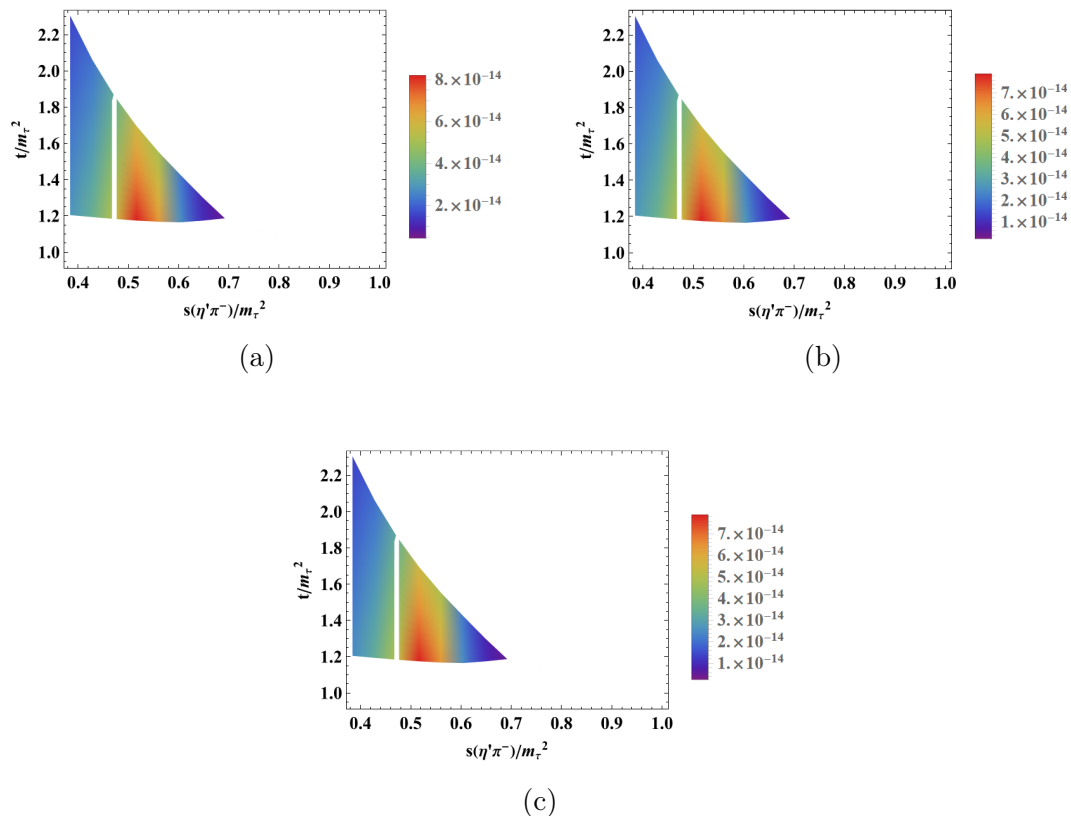


Figure 5.1: Dalitz plot distributions of $|\mathcal{M}|^2$ for the decay $\tau^- \rightarrow \pi^- \eta' \nu_\tau$. The figures show the distributions for the (a) Standard Model ($\hat{\epsilon}_S = \hat{\epsilon}_T = 0$), (b) $\hat{\epsilon}_S = 0.006$, $\hat{\epsilon}_T = 0$, and (c) $\hat{\epsilon}_S = 0$, $\hat{\epsilon}_T = 0.3$.

The triangular shape of the plots corresponds to the kinematic constraints of the decay process. Regions with higher values of $|\mathcal{M}|^2$ may indicate resonant behavior, influenced by intermediate states contributing to the decay amplitude.

Upon closer inspection, both scalar and tensor interactions alter the distribution of SM $|\mathcal{M}|^2$, but these effects are not significantly distinct. The tensor interaction does not appear to have a more pronounced effect compared to the scalar interaction in the provided plots. Both interactions cause a similar shift and spread in the distribution of $|\mathcal{M}|^2$, suggesting comparable magnitudes of impact on this decay channel. The color legends on the right of the plots represent the magnitude of $|\mathcal{M}|^2$, with higher values indicating more likely decay regions.

The shape and concentration of high-value regions provide insights into how the decay dynamics are influenced by different interaction terms. In this case, both scalar and tensor couplings have a noticeable but similar impact on the decay distribution.

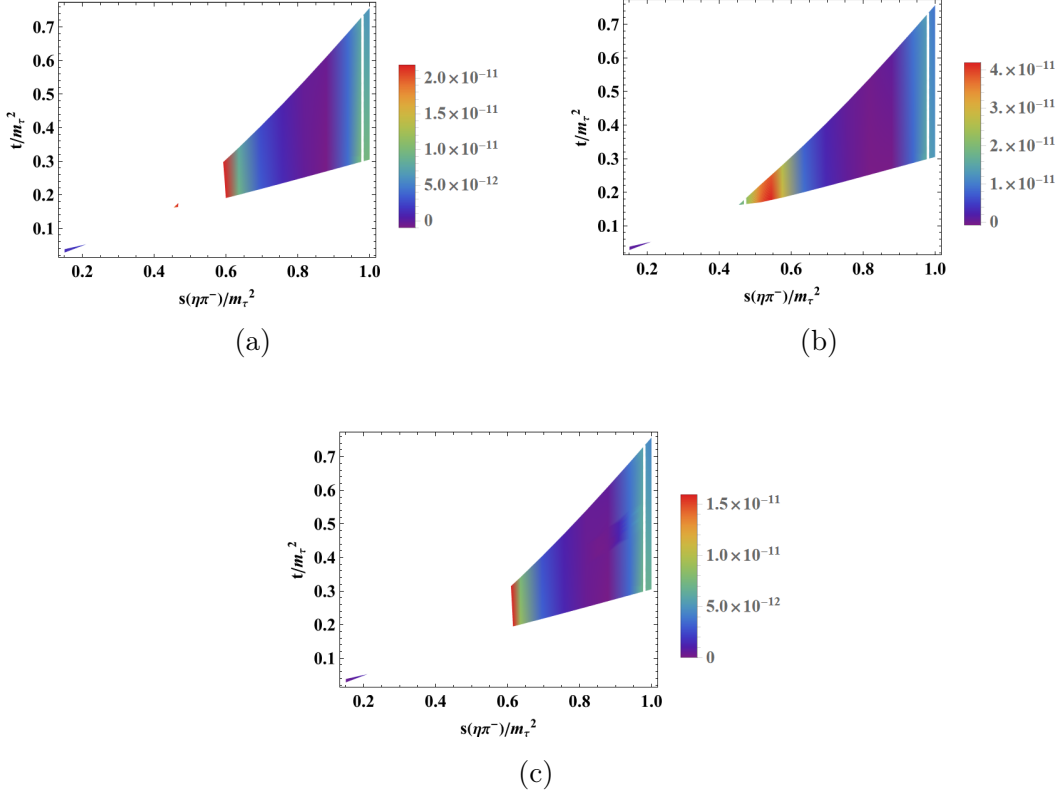


Figure 5.2: Dalitz plot distributions of $|\mathcal{M}|^2$ for the decay $\tau^- \rightarrow \pi^- \eta \nu_\tau$. The figures show the distributions for the (a) Standard Model ($\hat{e}_S = \hat{e}_T = 0$), (b) $\hat{e}_S = 0.002, \hat{e}_T = 0$, and (c) $\hat{e}_S = 0, \hat{e}_T = 0.3$.

Figure 5.2 shows the Dalitz plot distributions of $|\mathcal{M}|^2$ for the decay $\tau^- \rightarrow \pi^- \eta \nu_\tau$, as discussed in subsection (4.5.1). The plots depict the squared matrix element $|\mathcal{M}|^2$ as a function of s and t variables, each representing different scenarios with varying scalar and tensor coefficients:

1. Figure 5.2(a) represents the SM scenario without new physics contributions $\hat{e}_S = \hat{e}_T = 0$.
2. Figure 5.2(b) shows $|\mathcal{M}|^2$ distribution with a scalar coefficient $\hat{e}_S = 0.002$, while $\hat{e}_T = 0$, introducing a scalar interaction.

3. Figure 5.2(c) depicts $|\mathcal{M}|^2$ distribution with a tensor coefficient $\hat{\epsilon}_T = 0.3$, and $\hat{\epsilon}_S = 0$, introducing a tensor interaction.

On the x-axis, s is the invariant mass of the $\pi^-\eta$ system and on the y-axis, t represents the squared momentum transfer, both the variables are normalized to m_τ^2 . In 5.2(a), the plot shows the distribution of $|\mathcal{M}|^2$ with respect to the Mandelstam variables s and t . The distribution is mostly smooth, indicating the expected behavior without any additional contributions from scalar or tensor interactions. In 5.2(b), the distribution of $|\mathcal{M}|^2$ changes significantly. The shape becomes more extended along the s axis (the $\eta\pi^-$ invariant mass squared) while also maintaining some spread along the t axis. The distribution still maintains a smooth gradient but shows higher values overall compared to the SM case. This suggests that the scalar interaction enhances the decay amplitude. In 5.2(c), the plot shows a different distribution pattern. This indicates that the tensor interaction does not enhance the decay amplitude as much as the scalar interaction does in the given range of coefficients.

Δ	$\hat{\epsilon}_S(\hat{\epsilon}_T = 0)$	$\hat{\epsilon}_T(\hat{\epsilon}_S = 0)$	$\hat{\epsilon}_S$	$\hat{\epsilon}_T$
$\pi\eta'$				
Babar	$[-1.13, 0.68] \times 10^{-2}$	$ \hat{\epsilon}_T < 11.4$	$[-1.13, 0.67] \times 10^{-2}$	$[-11.9, 11.9]$
Belle	$[-1.07, 0.60] \times 10^{-2}$	$ \hat{\epsilon}_T < 10.6$	$[-1.06, 0.61] \times 10^{-2}$	$[-11.0, 11.0]$
Belle II	$[-4.8, 2.3] \times 10^{-3}$	$[-1.35, 1.41]$	$[-4.8, -4.3] \times 10^{-3}$	$[-3.4, -2.7]$
$\pi\eta$				
Babar	$[-8.3, 3.9] \times 10^{-3}$	$[-0.43, 0.39]$	$[-0.83, 0.37] \times 10^{-2}$	$[-0.55, 0.50]$
Belle	$[-7.7, 2.9] \times 10^{-3}$	$[-0.51, 0.47]$	$[-0.75, 0.29] \times 10^{-2}$	$[-0.48, 0.43]$
CLEO	$[-9.5, 5.0] \times 10^{-3}$	$[-0.62, 0.57]$	$[-0.95, 0.49] \times 10^{-2}$	$[-0.66, 0.60]$
Belle II	$[-4.8, 2.0] \times 10^{-3}$	$[-0.12, 0.08]$	$[-4.9, -4.3] \times 10^{-3}$	$[-0.20, -0.25]$

Table 5.1: The present upper limits on branching fractions, along with hypothetical observations with 20% precision from the Belle II experiment, provide constraints on scalar and tensor couplings [26].

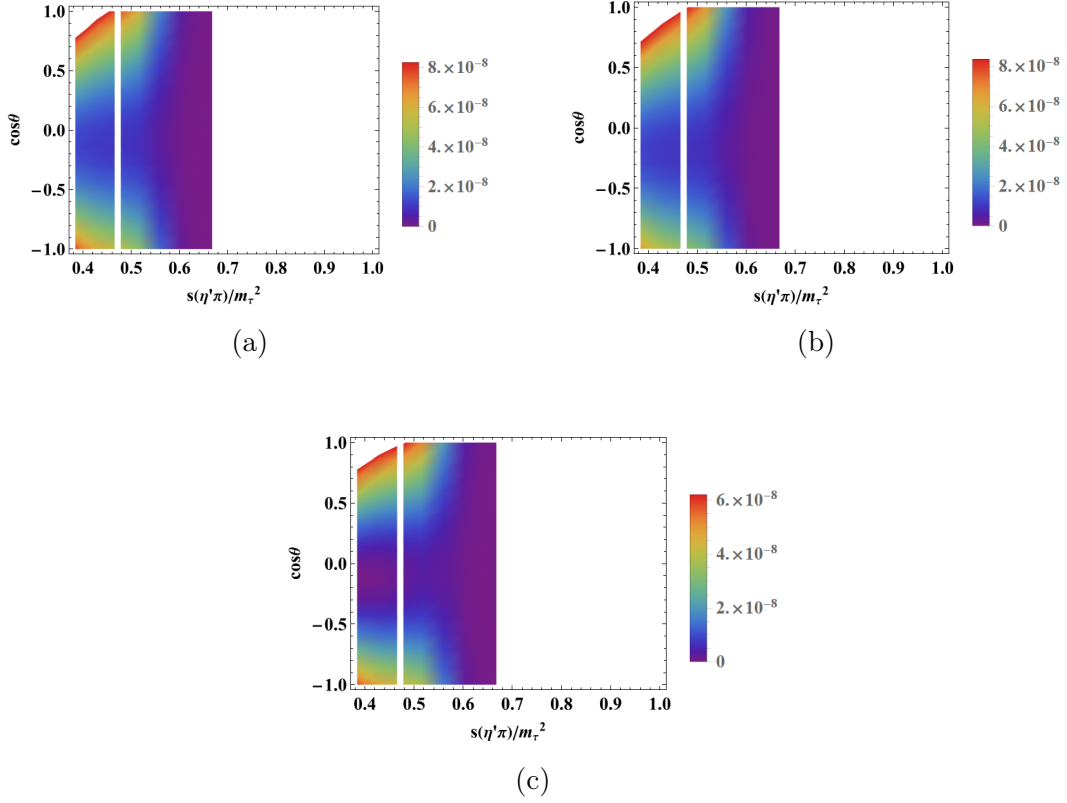


Figure 5.3: Differential decay width distributions for the decay $\tau^- \rightarrow \pi^- \eta' \nu_\tau$ in $(s, \cos \theta)$ variables. The figures show the distributions for the (a) Standard Model ($\hat{\epsilon}_S = \hat{\epsilon}_T = 0$), (b) $\hat{\epsilon}_S = 0.006$, $\hat{\epsilon}_T = 0$, and (c) $\hat{\epsilon}_S = 0$, $\hat{\epsilon}_T = 0.3$.

Figure 5.3 shows the distribution of differential decay width for the decay $\tau^- \rightarrow \pi^- \eta' \nu_\tau$, as per equation (4.35). The plots depict the double differential decay width normalized to τ width, as a function of the $(s, \cos \theta)$ variables, each representing different scenarios with varying scalar and tensor coefficients:

1. Figure 5.3(a) represents the SM scenario without new physics contributions $\hat{\epsilon}_S = \hat{\epsilon}_T = 0$.
2. Figure 5.3(b) shows distribution with a scalar coefficient $\hat{\epsilon}_S = 0.006$, while $\hat{\epsilon}_T = 0$.
3. Figure 5.3(c) depicts distribution with a tensor coefficient $\hat{\epsilon}_T = 0.3$, and $\hat{\epsilon}_S = 0$.

The Dalitz plot analysis for the decay $\tau^- \rightarrow \pi^- \eta' \nu_\tau$ across three scenarios shows that the overall distribution shape remains consistent. This consistency is observed

in all three cases: the SM scenario, as well as scenarios with different values of \hat{e}_S and \hat{e}_T (specifically, $\hat{e}_S = 0.006$ and $\hat{e}_T = 0$, $\hat{e}_S = 0$ and $\hat{e}_T = 0.3$). These findings show that, despite variations in interaction parameters, the underlying kinematics governing the decay process remain constant. Nevertheless, variations in the intensity across different regions of the plot indicate that the inclusion of the \hat{e}_S and \hat{e}_T parameters modify the dynamics of the decay process, resulting in a distinct distribution of events.

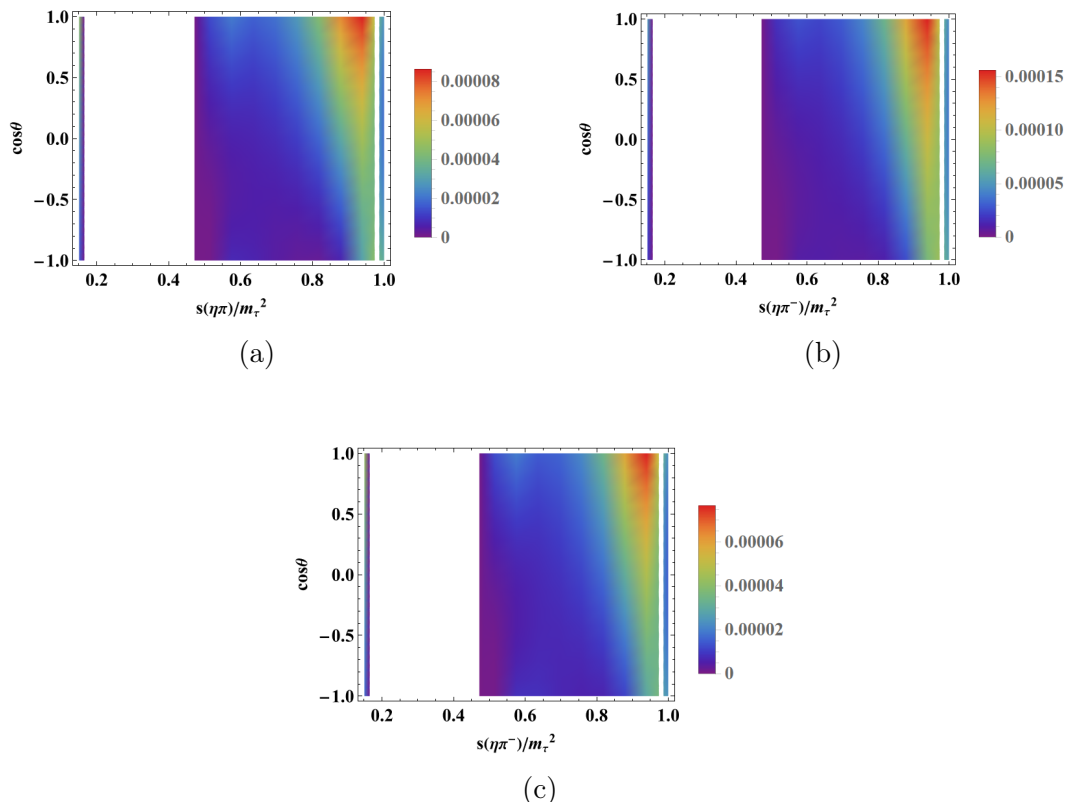


Figure 5.4: Differential decay width distributions for the decay $\tau^- \rightarrow \pi^- \eta \nu_\tau$ in $(s, \cos \theta)$ variables. The figures show the distributions for the (a) Standard Model ($\hat{e}_S = \hat{e}_T = 0$), (b) $\hat{e}_S = 0.002, \hat{e}_T = 0$, and (c) $\hat{e}_S = 0, \hat{e}_T = 0.3$.

Figure 5.4 shows the distribution of differential decay width for the decay $\tau^- \rightarrow \pi^- \eta \nu_\tau$, as per equation (4.35). The plots depict the double differential decay rate normalized to τ width, as a function of the $(s, \cos \theta)$ variables, each representing different scenarios with varying scalar and tensor coefficients:

1. Figure 5.4(a) represents the SM scenario without new physics contributions $\hat{e}_S = \hat{e}_T = 0$.

2. Figure 5.4(b) shows distribution with a scalar coefficient $\hat{\epsilon}_S = 0.002$, while $\hat{\epsilon}_T = 0$.
3. Figure 5.4(c) depicts distribution with a tensor coefficient $\hat{\epsilon}_T = 0.3$, and $\hat{\epsilon}_S = 0$.

The Dalitz plot analysis for the decay $\tau^- \rightarrow \pi^- \eta' \nu_\tau$ across three scenarios shows that the overall distribution shape remains consistent. This consistency is observed in all three cases: the SM scenario, as well as scenarios with different values of $\hat{\epsilon}_S$ and $\hat{\epsilon}_T$ (specifically, $\hat{\epsilon}_S = 0.002$ and $\hat{\epsilon}_T = 0$, $\hat{\epsilon}_S = 0$ and $\hat{\epsilon}_T = 0.3$). These findings show that, despite variations in interaction parameters, the underlying kinematics governing the decay process remain constant. Nevertheless, variations in the intensity across different regions of the plot indicate that the inclusion of the $\hat{\epsilon}_S$ and $\hat{\epsilon}_T$ parameters modify the dynamics of the decay process, resulting in a distinct distribution of events. The $\rho(770)$ meson resonance contributes negligibly in all the Dalitz plots as it is seen around 0.2 to 0.3 region and the region around 0.6 GeV shows the scalar meson $a_0(1450)$ resonance contribution. We have observed that Dalitz plot distribution examined in terms of both s , t variables and s , $\cos\theta$ variables exhibit limited sensitivity to realistic non-zero values of $\hat{\epsilon}_S$ and $\hat{\epsilon}_T$. These values are consistent with the present limits on branching fractions as given in Table 5.1.

5.2 Differential Decay Rate Analysis

The hadronic invariant mass distribution, as given by eq: (4.36), is plotted for $\tau^- \rightarrow \pi^- \eta \nu_\tau$ and $\tau^- \rightarrow \pi^- \eta' \nu_\tau$ decays in Figures 5.5 and 5.6, respectively. In the following, we analyze the two reactions individually.

5.2.1 Analysis of $\tau^- \rightarrow \pi^- \eta \nu_\tau$ Decay

In Figure 5.5, we illustrate the distribution of the total differential decay rate normalized to the τ width for $\tau^- \rightarrow \pi^- \eta \nu_\tau$ decay. The x-axis represents the invariant mass squared s (GeV^2), and the y-axis represents the normalized differential decay width $\frac{1}{\Gamma_\tau} \frac{d\Gamma}{ds}$ (GeV^{-2}). The decay widths are plotted as functions of the invariant mass squared s for three scenarios:

- Standard Model (SM): Scalar and tensor new physics coefficients are zero ($\hat{\epsilon}_S = \hat{\epsilon}_T = 0$).
- Scenario 1 (S1): $\hat{\epsilon}_S = 0.005$, $\hat{\epsilon}_T = 0$.
- Scenario 2 (S2): $\hat{\epsilon}_S = 0$, $\hat{\epsilon}_T = 0.3$

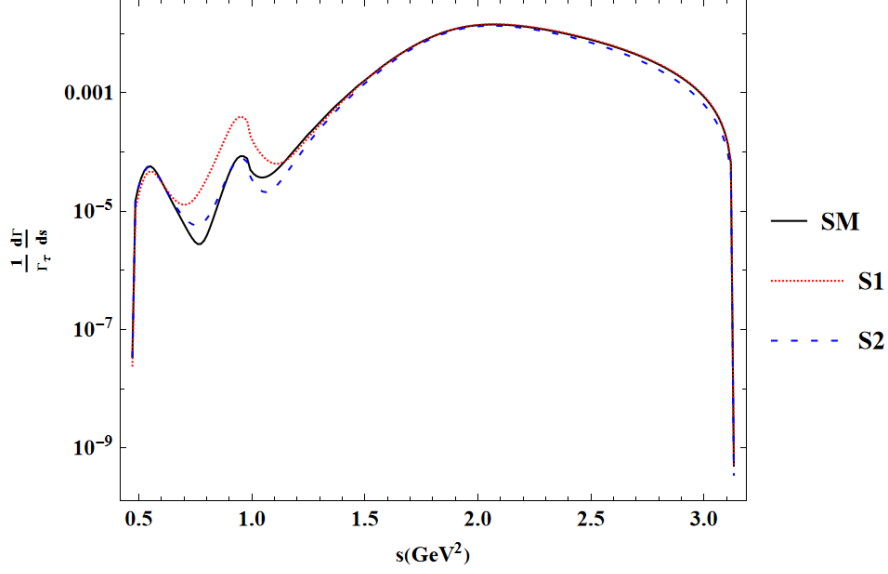


Figure 5.5: Distribution of the total differential decay width for $\tau^- \rightarrow \pi^- \eta \nu_\tau$ plotted against the invariant mass. The SM utilizes a Breit-Wigner formula using two resonances (black line), while scenarios with $\hat{e}_S = 0.005, \hat{e}_T = 0$ are represented by a red dotted line, and $\hat{e}_S = 0, \hat{e}_T = 0.3$ by a blue dashed line.

The plot shows several peaks in the distribution, notably around 0.7 GeV^2 and 1.0 GeV^2 . SM and S2 scenarios show similar peak structures. S1 scenario exhibits a significantly higher peak around 1.0 GeV^2 compared to SM and S2. The increase in the peak around 1.0 GeV^2 suggests that the scalar couplings significantly enhance the decay rate in this region compared to the SM. The tensor couplings do not significantly alter the decay width compared to the SM across most of the s range, except for a slight deviation near the peaks. These peaks likely correspond to resonance effects. These resonances are due to intermediate states in the decay process, such as meson resonances that decay into $\pi^- \eta$. For example, the peak around 1.0 GeV^2 might be associated with the $a_0(980)$ meson resonance. A clear peak around 0.59 GeV^2 is associated with $\rho(770)$ resonance, indicating its presence in the vector form factor, and the smaller rise observed near 2 GeV^2 might be observed due to resonances $a_0(1450)$ or $\rho(1450)$. Beyond 1.5 GeV^2 , the curves start to converge, with minimal differences at higher s values. At higher s values (near 3.0 GeV^2), all three scenarios converge, indicating the new physics effects are more prominent at lower s values. The convergence of the curves at higher s values indicates that new physics effects are less significant at these higher invariant mass squared values, possibly due to phase space limitations or the diminishing influence of resonances.

5.2.2 Analysis of $\tau^- \rightarrow \pi^- \eta' \nu_\tau$ Decay

In Figure 5.6, the distribution of the total differential decay width for $\tau^- \rightarrow \pi^- \eta' \nu_\tau$ decay as the function of invariant mass is presented. Notably, the substantial mass of the η' results in a reduced available phase space compared with the $\pi^- \eta$ mode. The x-axis represents the invariant mass squared s (GeV^2), and the y-axis represents the normalized differential decay width $\frac{1}{\Gamma_\tau} \frac{d\Gamma}{ds}$ (GeV^{-2}). The decay widths are plotted as functions of the invariant mass squared s for three scenarios:

- Standard Model (SM): Scalar and tensor new physics coefficients are zero ($\hat{\epsilon}_S = \hat{\epsilon}_T = 0$).
- Scenario 1 (S1): $\hat{\epsilon}_S = 0.005, \hat{\epsilon}_T = 0$.
- Scenario 2 (S2): $\hat{\epsilon}_S = 0, \hat{\epsilon}_T = 0.3$

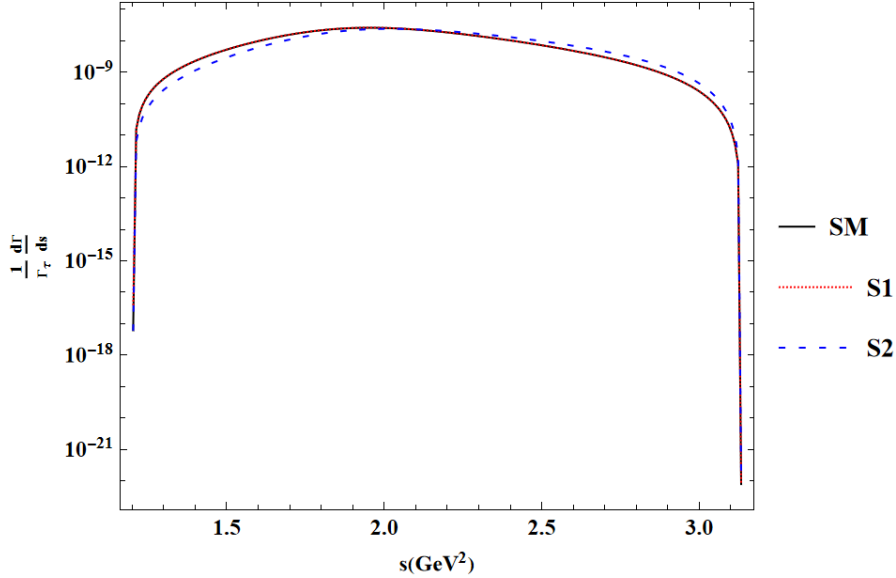


Figure 5.6: The figure depicts the distribution of the invariant mass of the $\eta' \pi^-$ system for the Standard Model (black line) and scenarios with $\hat{\epsilon}_S = 0.005, \hat{\epsilon}_T = 0$ (red dotted line), and $\hat{\epsilon}_S = 0, \hat{\epsilon}_T = 0.3$ (blue dashed line). The axes are scaled in units of GeV^2 .

For the $\tau^- \rightarrow \pi^- \eta' \nu_\tau$ decay, the scalar interactions show only a slight enhancement. The plot shows a prominent peak around 2.0 GeV^2 , with all scenarios (SM, S1, and S2) displaying similar behavior, though S2 shows slight deviations from the SM, particularly around the peak. The scalar interaction (S1) slightly enhances the peak, indicating some influence of scalar contributions in this region,

but not as prominently as in the $\tau^- \rightarrow \pi^- \eta \nu_\tau$ decay. $a_0(980)$ resonance appears at $s \approx 0.96 \text{ GeV}^2$, there is slight enhancement observed in the S1 scenario. The vector contribution experiences suppression due to the production threshold for $\pi^- \eta'$ occurring well beyond the region influenced by possible $\rho(770)$ effects. $\rho(1450)$ or $a_0(980)$ resonance region occurs at $s \approx 2.10 \text{ GeV}^2$. This region shows contributions and deviations in the S2 scenario. Both decay processes show that new physics effects are more pronounced around specific s values, particularly at lower to intermediate s regions. All scenarios (SM, S1, S2) tend to converge at high s values, suggesting that the influence of new physics diminishes at higher invariant mass squared values.

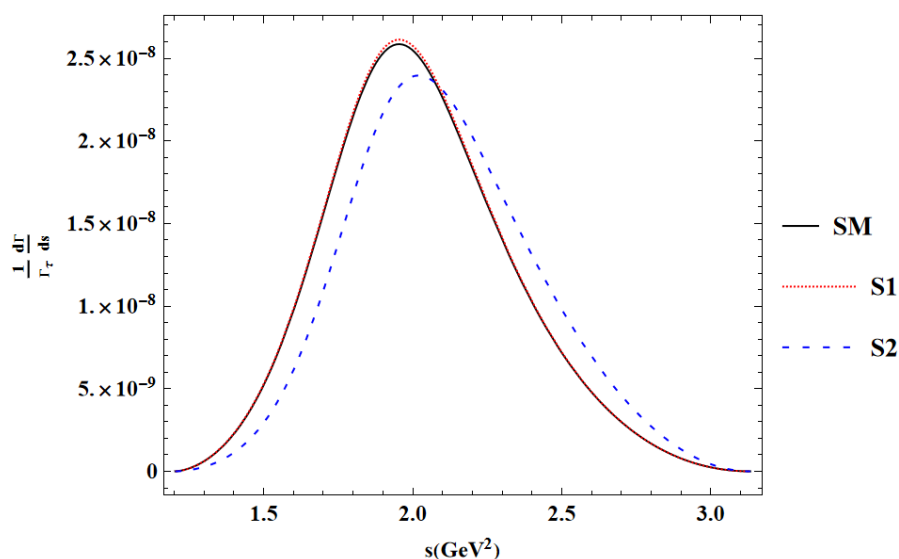


Figure 5.7: The figure depicts the distribution of the invariant mass of the $\eta'\pi^-$ system for the Standard Model (black line) and scenarios with $\hat{\epsilon}_S = 0.005, \hat{\epsilon}_T = 0$ (red dotted line), and $\hat{\epsilon}_S = 0, \hat{\epsilon}_T = 0.3$ (blue dashed line). The axes are scaled in units of GeV^2 .

The analysis of the differential decay widths for $\tau^- \rightarrow \pi^- \eta \nu_\tau$ and $\tau^- \rightarrow \pi^- \eta' \nu_\tau$ decays reveals the contributions of scalar and vector resonances. The peaks in the plots correspond to the resonances $a_0(980)$, $a_0(1450)$, $\rho(770)$, and $\rho(1450)$. The deviations observed in the S1 and S2 scenarios highlight the influence of scalar and tensor new physics interactions on these resonances. Focusing on these resonance regions in experimental data can provide insights into the presence and nature of new physics interactions.

5.3 Forward-Backward Asymmetry Analysis

This analysis is based on the observable $A_{FB}^{\pi^-\eta^{(\prime)}}$, discussed in subsection (4.5.4). The figure 5.8 illustrates three distinct scenarios regarding the A_{FB} prediction for $\tau^- \rightarrow \pi^-\eta'\nu_\tau$ decay, each representing potential deviations from the SM case. On the x-axis, s is the invariant mass of the $\pi^-\eta'$ system and A_{FB} on the y-axis represents the forward-backward asymmetry. Firstly, the black line represents the SM-based prediction of forward-backward asymmetry. The A_{FB} starts high at low s values, peaking sharply and then gradually decreasing. It shows a characteristic peak around 1.2 GeV² and then a smooth decline indicating the dynamics of the SM contributions. Secondly, depicted by the red line, Scenario 1 (S1) signifies a deviation from the SM, featuring a scalar coefficient of 0.002. When only the scalar coefficient is non-zero, the asymmetry is higher across the s range compared to the SM. The peak is more pronounced and occurs slightly earlier than in the SM case. It indicates that the scalar interaction increases the overall asymmetry and affects the low- s region more significantly.

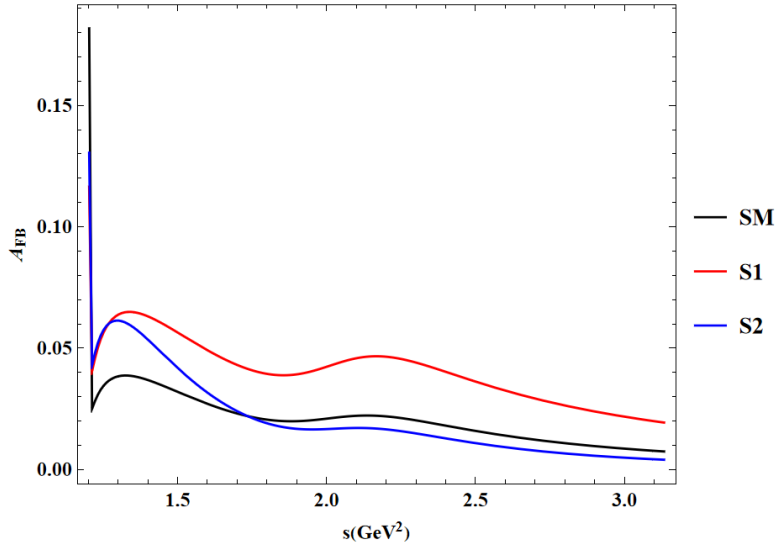


Figure 5.8: Comparison of A_{FB} for the decay $\tau^- \rightarrow \pi^-\eta'\nu_\tau$ for $\hat{e}_S = 0.002, \hat{e}_T = 0$ (red line) and for $\hat{e}_S = 0, \hat{e}_T = 0.3$ (blue line) against the Standard Model prediction (black line).

Thirdly, illustrated by the blue line, Scenario 2 (S2) presents another deviation from the SM case, characterized by a tensor coefficient of 0.3. When only the tensor coefficient is non-zero, the asymmetry has a similar initial behavior to the SM but is slightly lower across most of the s range. The tensor interaction affects

the overall shape, making the peak slightly broader and the subsequent decline more gradual compared to the SM.

The forward-backward asymmetry plots provide insights into the dynamics of the decay and the effects of new physics interactions. Scalar and tensor interactions both modify the asymmetry but in different ways, with scalars generally increasing the magnitude of asymmetry and tensors altering the shape of the asymmetry distribution. These distinctions in the plotted forward-backward asymmetry among the SM and alternative scenarios (S1 and S2) denote potential indications of new physics in the decay $\tau^- \rightarrow \pi^- \eta' \nu_\tau$.

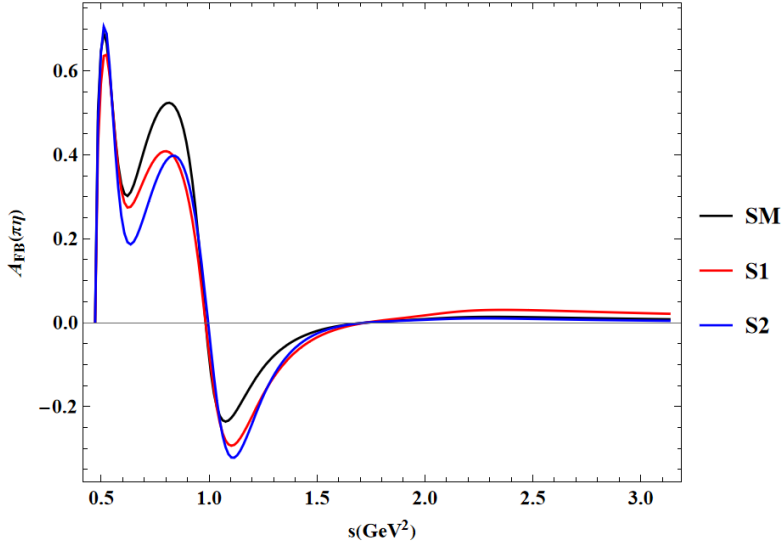


Figure 5.9: Comparison of A_{FB} for the decay $\tau^- \rightarrow \pi^- \eta \nu_\tau$ with $\hat{\epsilon}_S = 0.002$, $\hat{\epsilon}_T = 0$ (red line) and $\hat{\epsilon}_S = 0$, $\hat{\epsilon}_T = 0.3$ (blue line) against the Standard Model prediction (black line).

The fig. 5.9 illustrates three distinct scenarios regarding the A_{FB} prediction for the decay $\tau^- \rightarrow \pi^- \eta \nu_\tau$, each representing deviations from the SM case. On the x-axis, s is the invariant mass of the $\pi^- \eta$ system and A_{FB} on the y-axis represents the forward-backward asymmetry.

SM (black line): The behavior of this curve is based on the SM predictions. The asymmetry shows two significant peaks followed by a deep valley below zero. The first peak occurs around $s \approx 0.5 \text{ GeV}^2$, reaching a value above 0.6. The second peak is lower, around $s \approx 1 \text{ GeV}^2$, and is followed by a sharp dip below zero, indicating a strong forward-backward asymmetry transition. As s increases further, A_{FB} gradually stabilizes around zero.

S1 (red line): This curve's behavior follows a theoretical model with $\hat{\epsilon}_S = 0.002$, $\hat{\epsilon}_T =$

0. When only the scalar coefficient is non-zero, the overall shape of A_{FB} is similar to the SM case but with notable differences. The first peak is lower than in the SM, indicating a reduced forward asymmetry in this region. The valley is deeper compared to the SM, showing a more pronounced backward asymmetry. This suggests that the scalar interaction modifies the asymmetry by reducing the forward asymmetry at the peak and enhancing the backward asymmetry at the valley.

S2 (blue line): This curve's behavior is based on a theoretical model where $\hat{\epsilon}_S = 0$, $\hat{\epsilon}_T = 0.3$. When only the tensor coefficient is non-zero, the initial peak is slightly higher than in the SM, indicating an increased forward asymmetry in this region. The second peak and the subsequent dip are more pronounced, with the valley being deeper than in the SM. This indicates that the tensor interaction enhances both the forward and backward asymmetry transitions more significantly than the scalar interaction. This might also suggest the existence of NP extending beyond the Standard Model. Observing these deviations experimentally could provide evidence for the presence of such interactions and contribute to our understanding of the underlying physics in τ decays.

Chapter 6

Conclusion

This thesis investigates the rare hadronic τ lepton decays, specifically $\tau^- \rightarrow \pi^- \eta^{(\prime)} \nu_\tau$, which are typically hindered by G-parity under the SM framework. Our study analyzed these decays within the framework of a comprehensive EFT, incorporating six-dimensional operators and considering left-handed neutrinos. We employed the scalar, vector, and tensor form factors within the frameworks of ChPT and RChT [38]. We then used these form factors to calculate a double differential decay distribution and depict the branching ratio for each decay. We then made Dalitz plots for three scenarios (SM case, scalar couplings, and tensor couplings) to determine which new physics coefficient effects decay the most. Finally, we calculated A_{FB} and plotted it to evaluate the disparities between the different scenarios. We have noticed that the impacts of non-standard interactions can be seen in the Dalitz Plots, hadronic invariant mass distribution, and A_{FB} . In this study, we gave predictions for various observables, including Dalitz plots, Branching Ratios (BR), and Forward-Backward Asymmetry. Our attention is directed towards evaluating their importance within the framework of NP scenarios.

- Dalitz plot distributions, examined in terms of both the Mandelstam variables s and t , as well as when t is substituted by the angle θ between the two charged particles, exhibit limited sensitivity to realistic non-zero values of \hat{e}_S and \hat{e}_T .
- Our analysis demonstrates that the BR experiences negligible reductions throughout the s range in the NP scenarios. Moreover, the NP scenarios largely align with the SM predictions, suggesting that BR might not be the most efficient indicator for NP prediction compared to other parameters.
- Our study shows that the inclusion of scalar and tensor couplings significantly alters the A_{FB} in $\tau \rightarrow \pi^- \eta^{(\prime)} \nu_\tau$ decays, revealing distinct deviations

from the SM predictions. This finding highlights the significance of A_{FB} in distinguishing between NP scenarios.

To summarize, the observables of $\tau \rightarrow \pi^- \eta^{(\prime)} \nu_\tau$ decay provide valuable insights into these decay mechanisms. Overall, our findings showed modifications and small deviations to some extent from the SM results when incorporating scalar and tensor new physics coefficients but to better understand and potentially observe these effects, it is crucial to obtain more precise and extensive datasets. Future experiments with higher precision and larger data samples, such as those expected from upgrades at the LHC experiments, will be crucial in advancing this research. Additionally, addressing theoretical uncertainties and refining models will help in making more accurate predictions and improving the sensitivity to new physics. Nonetheless, both theoretical inquiries and experimental investigations into these τ decay processes hold the potential to substantially improve our capacity for uncovering new physics phenomena in the future.

References

- [1] Suzanne van Dam. Spontaneous symmetry breaking in the higgs mechanism.
- [2] A. J. Buras. *Weak Hamiltonian, CP Violation and Rare Decays*.
- [3] D. G. Dumm, P. Roig, A. Pich, and J. Portoles. Tau \rightarrow pi pi pi nu_tau decays and the a_1(1260) off-shell width revisited. *Physics Letters B*, 684(2-3):236–241, 2010.
- [4] Zhiqing Zhang. Tau decays and s. *Nuclear and Particle Physics Proceedings*, 260:130–133, 2015. The 13th International Workshop on Tau Lepton Physics.
- [5] S. Weinberg. *Phys. rev.* 112:1375, 1958.
- [6] Rafael Escribano, Sergio González-Solís, and Pablo Roig. *JHEP* 1310, 039. *Journal of High Energy Physics*, 2013:039, 2013.
- [7] Rafael Escribano, Sergio González-Solís, Matthias Jamin, and Pablo Roig. *JHEP* 1409, 042. *Journal of High Energy Physics*, 2014:042, 2014.
- [8] Rafael Escribano, Sergio González-Solís, and Pablo Roig. *Phys. Rev. D* 94, no. 3, 034008. *Physical Review D*, 94(3):034008, 2016.
- [9] Y. Meurice. Restrictions on $\tau^- \rightarrow \eta\pi^- \nu$ in two higgs doublet models. *Physical Review D*, 36:2780, 1987. [INSPIRE].
- [10] S. Descotes-Genon and B. Moussallam. Analyticity of $\eta\pi$ isospin-violating form factors and the $\tau \rightarrow \eta\pi\nu$ second-class decay. *European Physical Journal C*, 74:2946, 2014. [arXiv:1404.0251] [INSPIRE].
- [11] P. del Amo Sanchez and others [BaBar Collaboration]. Studies of $\tau^- \rightarrow \eta K^- \nu_\tau$ and $\tau^- \rightarrow \eta\pi^- \nu_\tau$ at BaBar and a search for a second-class current. *Physical Review D*, 83:032002, 2011. [arXiv:1011.3917] [INSPIRE].
- [12] Belle Collaboration. Electroweak physics from Belle. In *Proceedings of the EPS International Conference on High Energy Physics (EPS-HEP 2009)*, page 374, 2009. [INSPIRE].

- [13] CLEO Collaboration. First observation of the decay $\tau^- \rightarrow K^- \eta \nu_\tau$. *Physical Review Letters*, 76:4119, 1996. [INSPIRE].
- [14] B. Aubert and et al. [BaBar Collaboration]. Measurement of the $\tau^- \rightarrow \eta \pi^- \pi^+ \pi^- \nu_\tau$ branching fraction and a search for a second-class current in the $\tau^- \rightarrow \eta'(958) \pi^- \nu_\tau$ decay. *Phys. Rev. D*, 77:112002, 2008. [INSPIRE].
- [15] Belle Collaboration, K. Hayasaka. Electroweak physics from Belle. In *PoS(EPS-HEP 2009)*, page 374. [INSPIRE].
- [16] T. Bergfeld and et al. [CLEO Collaboration]. First observation of $\tau \rightarrow 3\pi \eta \nu_\tau$ and $\tau \rightarrow f_1 \pi \nu_\tau$ decays. *Phys. Rev. Lett.*, 79:2406, 1997. [INSPIRE].
- [17] Belle-II Collaboration and B2TiP-Community. *Belle-II Physics Book*. to be published in.
- [18] Antonio Rodriguez-Sanchez. *Precision physics in Hadronic Tau Decays*. PhD thesis, Valencia U., 2018. Presented on 2018-10.
- [19] Antonio Pich. The Standard Model of Electroweak Interactions. In *2010 European School of High Energy Physics*, pages 1–50, 1 2012.
- [20] K. A. Olive and others [Particle Data Group Collaboration]. *Chin. phys. c* 38, 090001. 2014.
- [21] Antonio Pich. Precision tau physics. *Progress in Particle and Nuclear Physics*, 75:41–85, March 2014.
- [22] V. J. Martin. Lecture 13: Hadron decays, 2013. Accessed: 2024-06-24.
- [23] Matthias Neubert. *Effective Field Theory and Heavy Quark Physics*. World Scientific, 2005.
- [24] T. Bhattacharya et al. Probing novel scalar and tensor interactions from (ultra)cold neutrons to the lhc. *Phys. Rev. D*, 85:054512, 2012. [arXiv:1110.6448] [INSPIRE].
- [25] V. Cirigliano, J. Jenkins, and M. González-Alonso. Semileptonic decays of light quarks beyond the standard model. *Nucl. Phys. B*, 830:95, 2010. [arXiv:0908.1754] [INSPIRE].
- [26] E. Garcés, M. Hernández Villanueva, G. López Castro, et al. Effective-field theory analysis of the $\tau^- \rightarrow \eta(\eta') \pi^- \nu_\tau$ decays. *J. High Energ. Phys.*, 2017(27), 2017.

- [27] Antonio Pich. Effective Field Theory with Nambu-Goldstone Modes. 4 2018.
- [28] Aneesh V. Manohar. Effective field theories. In *10th Lake Louise Winter Institute: Quarks and Colliders*, pages 274–315, 6 1995.
- [29] Jürg Gasser and Heinrich Leutwyler. Chiral perturbation theory to one loop. *Annals of Physics*, 158(1):142–210, 1984.
- [30] Steven Weinberg. Phenomenological lagrangians. *Physica A: Statistical Mechanics and its Applications*, 96(1-2):327–340, 1979.
- [31] Gerhard Ecker, Jürg Gasser, and Heinrich Leutwyler. Effective lagrangians for quark and gluon interactions in a chiral framework. *Physics Letters B*, 223(3):425–431, 1989.
- [32] Antonio Dobado, A Gómez Nicola, and J R Peláez. Chiral symmetry at finite temperatures: Linear versus nonlinear realizations. *Physical Review D*, 56(1):451, 1997.
- [33] J. Portoles. Basics of Resonance Chiral Theory. *AIP Conf. Proc.*, 1322(1):178–187, 2010.
- [34] V. Cirigliano, G. Ecker, M. Eidemuller, A. Pich, and J. Portoles. The $\langle \text{VAP} \rangle$ Green function in the resonance region. *Phys. Lett. B*, 596:96–106, 2004.
- [35] J. Erler. Electroweak radiative corrections to semileptonic tau decays. *Rev. Mex. Fis.*, 50:200–202, 2004.
- [36] Johan Bijnens. Chiral perturbation theory. In *International Workshop on Nuclear and Particle Physics: Chiral Dynamics in Hadrons and Nuclei*, 2 1995.
- [37] S. Aoki et al. Review of lattice results concerning low-energy particle physics. *Eur. Phys. J. C*, 77:112, 2017. [arXiv:1607.00299] [INSPIRE].
- [38] R. Escribano, S. González-Solís, and P. Roig. Predictions on the second-class current decays $\tau^- \rightarrow \pi^- \eta(t) \nu_\tau$. *Physical Review D*, 94:034008, 2016. [arXiv:1601.03989] [INSPIRE].
- [39] M. Jamin, J. A. Oller, and A. Pich. Strange quark mass from tau- decay and SU(3) breaking. *Nucl. Phys. B*, 622:279, 2002.
- [40] T. Feldmann, P. Kroll, and B. Stech. *Phys. Lett. B* 449, 339. 1999.
- [41] F. Ambrosino et al. *Jhep* 0907, 105. 2009.

- [42] M. Fujikawa and others [Belle Collaboration]. Title of the paper. *Phys. Rev. D*, 78:072006, 2008.
- [43] S. Descotes-Genon and B. Moussallam. Analyticity of $\eta\pi$ isospin-violating form factors and the $\tau \rightarrow \eta\pi\nu$ second-class decay. *European Physical Journal C*, 74:2946, 2014.
- [44] Dao-Neng Gao. Angular distribution asymmetry in $\tau^- \rightarrow \pi^- \pi^0 \nu_\tau$ decay in the two-higgs-doublet model with large $\tan\beta$. *Physical Review D*, 71:051301, 2005.